

1 Diapycnal mixing and tracer dispersion in a 2 terrain-following coordinate model

3 Noémie Schifano¹, Clément Vic¹, Jonathan Gula^{1,2,3}, M. Jeroen Molemaker³,
4 James C. McWilliams³

5 ¹Univ Brest, CNRS, Ifremer, IRD, Laboratoire d'Océanographie Physique et Spatiale (LOPS), IUEM,
6 Plouzané, France

7 ²Institut Universitaire de France (IUF), Paris, France

8 ³Department of Atmospheric and Oceanic Sciences and Institute of Geophysics and Planetary Physics,
9 University of California, Los Angeles, CA 90095-1565, United States

10 Key Points:

- 11 • Diapycnal mixing is quantified in realistic high-resolution simulations using pas-
12 sive tracer experiments and online diagnostics of effective diapycnal mixing
- 13 • Effective diapycnal mixing is close to parameterized values over the abyssal plain
but can be larger above steep ridge slopes.
- 14 • Numerical mixing is minimized by smoothing topography and effective mixing aligns
closely with parameterized mixing even in the presence of tides.

17 **Abstract**

18 Diapycnal mixing, driven by small-scale turbulence, is crucial for global ocean circula-
19 tion, particularly for the upwelling of deep water masses.

20 However, accurately representing diapycnal mixing in ocean models is challenging
21 because numerical errors can introduce significant spurious mixing that complicates the
22 overall mixing representation.

23 In this study, we explore the diapycnal mixing in a high-resolution regional model
24 of the North Atlantic's subpolar gyre using the Coastal and Regional Ocean Commu-
25 nity model (CROCO), a terrain-following coordinate model widely used for regional ap-
26 plications. We explore challenging dynamical regimes involving energetic submesoscale
27 motions and high-frequency internal waves over the Reykjanes Ridge. We focus on how
28 different advection schemes and vertical resolutions affect numerical diapycnal mixing.
29 Our approach includes online diagnostics of buoyancy fluxes and Tracer Release Experi-
30 ments to quantify the effective mixing, which combines parameterized and numerical
31 diapycnal mixing.

32 Our key findings reveal that in flat regions, numerical mixing is minimal, and ef-
33 fective diapycnal mixing aligns with parameterized values. However, in areas with steep
34 topographies like the Reykjanes Ridge, numerical mixing can locally significantly exceed
35 parameterized mixing due to grid slope inconsistencies. While smoothing the topogra-
36 phy can mitigate this excessive mixing, it may also alter critical flow-topography inter-
37 actions. Additionally, higher vertical resolution reduces dispersive and diffusive effects,
38 bringing tracer-based diffusivities in line with effective diffusivities, though it also increases
39 numerical mixing in steep regions.

40 These results underscore the complex trade-offs in managing numerical mixing in
41 ocean models. Accurately representing diapycnal mixing requires balancing high reso-
42 lution with the control of numerical errors. Effective management involves careful con-
43 sideration of topographic smoothing and resolution adjustments. Future advancements
44 may benefit from innovative approaches like the Brinkman penalization to address these
45 challenges effectively.

46 **1 Introduction**

47 The low-frequency and large-scale ocean circulation is mostly adiabatic, as water
48 masses move predominantly along surfaces of constant density, or isopycnals. However,
49 diabatic processes, which involve mixing across isopycnals, are crucial for closing the gen-
50 eral circulation (de Lavergne et al., 2022). This diapycnal mixing shapes the lower limb
51 of the meridional overturning circulation (e.g., Stommel, 1958; Samelson & Vallis, 1997).
52 Recent theories of the abyssal circulation insist on the role of diapycnal mixing, and its
53 still partially uncovered space and time variability, in the upwelling of the heaviest wa-
54 ter masses (e.g., reviewed in de Lavergne et al., 2022).

55 Yet, diapycnal mixing remains difficult to map globally and statistically, because
56 its main driver is small-scale turbulence, which is patchy and intermittent by nature. The
57 most accurate estimate of diapycnal mixing is obtained by microstructure (very high fre-
58 quency) measurements of velocity shear (a review of the measurement techniques can
59 be found in Frajka-Williams et al., 2022). Indirect techniques for measuring diapycnal
60 mixing, such as Tracer Release Experiments (TRE), have been developed to assess the
61 intensity of mixing over different time and space scales (Ledwell & Watson, 1991). Di-
62 rect and indirect measurements have revealed the very large variability of diapycnal mix-
63 ing throughout the world's oceans (Ledwell et al., 1993, 2000; Naveira Garabato et al.,
64 2004; Kunze et al., 2006; Waterhouse et al., 2014).

The main energy sources for diapycnal mixing are tides and winds (Munk & Wunsch, 1998). They generate internal gravity waves that travel through the ocean before breaking, triggering diapycnal mixing. Successive refinements in the knowledge of the physics and energetics of internal waves have led to the development of parameterizations of diapycnal mixing, especially for global ocean circulation models that will not resolve internal gravity wave dynamics in a foreseeable future (e.g., Jayne & St Laurent, 2001; Olbers & Eden, 2013; de Lavergne et al., 2019, 2020; Alford, 2020).

In primitive-equation regional and global models that include tidal forcing and high-frequency atmospheric forcing, internal gravity waves and other small-scale processes leading to diapycnal mixing can be partially represented (e.g., Zilberman et al., 2009; Arbic et al., 2010; Gula et al., 2016; Vic et al., 2018; Mazloff et al., 2020; Thakur et al., 2022). Therefore, specific parameterizations for tidal (diapycnal) mixing cannot be used, and diapycnal mixing is often parameterized by turbulent closures that bridge the gap between internal wave activity and actual mixing. For example, using the K-profile parameterization (KPP, Large et al., 1994), one assumes that the represented internal waves produce sufficient vertical shear to trigger KPP's Richardson-based mixing, and a background diffusivity value is set to cover internal waves not resolved by the model. Conversely, KPP influences the representation of internal waves (Thakur et al., 2022).

In addition to the parameterized mixing, advection schemes produce additional mixing, often undesired, sometimes called ‘numerical’ or ‘spurious’ mixing (Griffies et al., 1998, 2000; Lee et al., 2002; Hofmann & Morales Maqueda, 2006; Burchard & Rennau, 2008; Marchesiello et al., 2009; Hecht, 2010; Hill et al., 2012; Bracco et al., 2018; Megann, 2018). This numerical mixing is an important issue because it includes a diapycnal component that potentially exceeds the parameterized mixing, sometimes by several orders of magnitude (Bracco et al., 2018). Its intensity is determined by the accuracy of the advection schemes, the horizontal and vertical resolution, and the type of the coordinate system (geopotential, isopycnal, or terrain-following coordinates). Strategies have been designed to minimise the diapycnal part of the numerical mixing by rotating it along isoneutral surfaces (Griffies et al., 1998), with solutions specifically designed for terrain-following coordinates (Marchesiello et al., 2009; Lemarié et al., 2012). However, the impact of such solutions on the effective diapycnal mixing has rarely been quantified for regional submesoscale-permitting or submesoscale-resolving models, especially in the presence of tides and other high-frequency motions. If one wants to use a primitive equation model specifically to study diabatic processes, and their impact on water mass transformation and deep ocean circulation, one cannot ignore mixing due to advection schemes.

In the present study, we aim to quantify the diapycnal mixing due to different advection schemes routinely used in the Coastal and Regional Ocean Community model (CROCO), based on the Regional Oceanic Modelling System (ROMS, A. F. Shchepetkin & McWilliams, 2005). We pay particular attention to how the advection schemes, in combination with different vertical resolutions, affect the representation of passive tracers. The sensitivity of the simulated ocean dynamics to the vertical grid resolution has been addressed in relatively coarse global and basin-wide models, and important consequences for water mass representation, the overturning circulation, and energy fluxes have been pointed out (Stewart et al., 2017; Xu et al., 2023).

We set up a regional configuration in the subpolar North Atlantic Gyre, which includes part of the Reykjanes Ridge and the Iceland Basin. This region is of particular interest because it is located at the gateway of dense water formation (Piron et al., 2017) and has several sources of turbulence due to strong wind events and flow-topography interactions (Vic et al., 2021). The numerical mixing is estimated using a novel ad hoc online diagnostic and passive tracer release experiments (TREs). While the former allows us to precisely quantify the pointwise extra mixing due to the numerical schemes, the latter are a useful tool to visually capture the specific features of each scheme, and also to independently quantify the amount of mixing experienced by a tracer over different

physical and numerical conditions. We also argue that the tracers can be seen as localized patches of biological or geochemical material to illustrate how the tracers' behavior is affected by numerical choices.

The plan is as follows. In section 2, we present the model configuration and the set of simulations we designed to investigate the impact of numerical choices on diapycnal mixing. We also present the different methods used to quantify diapycnal mixing, online, and based on the TREs. In section 3, we present an overview of the simulated dynamics along with a comparison of the simulated mixing with in situ estimates from microstructure data. We then compare the different estimates of diapycnal mixing (parameterized vs diagnosed following the different methods) in different regions, over smooth vs steep and rough topography. The impact of the advection schemes on the tracer representation is illustrated. In section 4 we summarize the results and discuss the limitations of the methods as well as the implications of our findings.

2 Methods

2.1 Numerical set up

We perform three-dimensional realistic simulations using the ocean model CROCO (Auclair et al., 2022). CROCO has been developed on the basis of ROMS (A. F. Shchepetkin & McWilliams, 2005) and still shares a significant amount of code, in particular most of the numerical options detailed below. It solves the primitive equations and uses terrain-following (sigma) coordinates. We use the hydrostatic version of the code. The model domain covers part of the Reykjanes Ridge, south of Iceland, and part of the Iceland Basin to its east (Figure 1). The model grid has 1000×800 points on the horizontal with a grid spacing of 800 m, and the number of vertical levels varies between 50 and 200 across the set of simulations (Section 2.2 and Table 1). The horizontal resolution is among the standards in the regional modelling community, and allows to resolve the mesoscales and partially resolve the submesoscales and the internal gravity wave continuum (e.g., Arbic, 2022). All simulations are run with a time step of 80 seconds.

The model bathymetry is based on the 15-second resolution Shuttle Radar Topography Mission dataset (SRTM15.PLUS, Tozer et al., 2019). The raw bathymetry is smoothed with a Gaussian kernel with a radius of 5 grid points to avoid steep gradients that could lead to pressure gradient errors (A. F. Shchepetkin & McWilliams, 2003). The steepness parameter does not exceed $r = 0.2$ (Beckmann & Haidvogel, 1993).

Atmospheric forcing is provided at hourly resolution by the Climate Forecast System Reanalysis (CFSR, Saha et al., 2010). Initial and boundary conditions are provided by a parent simulation covering the entire Atlantic Ocean at 3-km resolution, GIGATL3 (Gula et al., 2021). The parent simulation includes barotropic and baroclinic tides. Thus, the tidal forcing is embedded in the boundary conditions at hourly resolution. We initialize the simulations in Aug 2008 and run them for 2 months.

The subgrid scale mixing is parameterised using the KPP scheme (Large et al., 1994). KPP is a turbulent closure of scalars and momentum that provides the vertical eddy diffusivity coefficient K_{KPP} . In the surface and bottom layers, which are calculated based on a critical bulk Richardson number, K_{KPP} is the product of the boundary layer thickness h_{bl} , a turbulent velocity scale w_S and a shape function G , both of which depend on the vertical coordinate σ :

$$K_{KPP} = h_{bl} w_S(\sigma) G(\sigma). \quad (1)$$

In the interior, outside these layers, K_{KPP} is calculated as the sum of three processes: Background internal wave breaking, vertical shear instability, and convective instability. Background internal wave breaking is parameterized with a constant background diffusivity ($K^w = 10^{-5} \text{ m}^2 \text{ s}^{-1}$).

166 Vertical shear instability is parameterized using the Richardson number $Ri = N^2/S^2$,
 167 where N^2 is the buoyancy frequency squared and $S^2 = \left(\frac{\partial u}{\partial z}\right)^2 + \left(\frac{\partial v}{\partial z}\right)^2$ is the squared
 168 vertical shear of the horizontal velocity, using the same formulation than in Large et al.
 169 (1994):

$$K^S = \begin{cases} \nu^0 & Ri < 0 \\ \nu^0 \left[1 - \left(\frac{Ri}{Ric}\right)^2\right]^3 & 0 < Ri < Ric \\ 0 & Ric < Ri \end{cases}$$

170 with a critical Richardson number $Ric = 0.7$ and $\nu^0 = 5 \times 10^{-3} \text{ m}^2 \text{ s}^{-1}$. In case of
 171 convective instability ($N^2 \leq 0$), an additional diffusivity $K^C = 10^{-1} \text{ m}^2 \text{ s}^{-1}$ is added.

172 All of the simulations presented below use the same third order upwind scheme (UP3)
 173 for momentum advection in the horizontal (A. F. Shchepetkin & McWilliams, 2005). Hor-
 174 izontal advection schemes for active tracers (potential temperature and salinity) are split
 175 and rotated upstream biased schemes of the third (RSUP3) or fifth order (RSUP5) de-
 176 pending on the experiments, with the rotation oriented along isoneutral surfaces (Lemarié
 177 et al., 2012). The vertical advection of momentum and active tracers uses a fourth-order
 178 centered parabolic spline reconstruction (SPLINES), with an adaptive, Courant-number-
 179 dependent implicit scheme (A. F. Shchepetkin, 2015).

180 The advection of passive tracers uses either the same schemes as for active trac-
 181 ers (RSUP3 or RSUP5 in the horizontal, and SPLINES in the vertical) or a 5th-order
 182 Weighted Essentially Non-Oscillatory scheme (WENO5, Jiang & Shu, 1996) in all di-
 183 rections. The WENO5 scheme is a common choice for biogeochemical tracers, mainly
 184 because it limits oscillations and the negative concentrations. Therefore, it is important
 185 to assess how it affects numerical mixing as it would affect the global cycles of biogeo-
 186 chemical tracers. The different combinations of schemes for our sensitivity studies are
 187 summarized below.

188 2.2 Set of simulations

189 We focus here on two parameters that affect numerical mixing: the vertical reso-
 190 lution and the choice of advective schemes. The vertical resolution depends on the num-
 191 ber of σ -levels and the local bathymetry (Appendix A). We tested the sensitivity of mix-
 192 ing in simulations with 50, 100 and 200 vertical levels. While the use of 50 levels (or less)
 193 has long been in the range of the community standards (e.g., Marchesiello et al., 2003;
 194 Penven et al., 2005), the use of ≈ 100 levels has become routine to better represent current-
 195 topography interactions (e.g., Molemaker et al., 2015; Gula et al., 2016, 2019; Vic et al.,
 196 2018). The use of 200 levels is significantly more computationally expensive, but, as shown
 197 in the results section, provides important improvements in the representation of passive
 198 tracers.

199 We use three combinations of advective schemes (listed in Table 1):

- 200 • The rsup3 combination uses RSUP3 in the horizontal and SPLINES in the ver-
 201 tical for active and passive tracers
- 202 • The rsup5 combination uses RSUP5 in the horizontal and SPLINES in the ver-
 203 tical for active and passive tracers
- 204 • The weno5 combination uses RSUP5 and SPLINES for active tracers, and WENO5
 205 in the horizontal and vertical for passive tracers.

206 Each combination is run with 50, 100, and 200 vertical levels. Each simulation is
 207 labelled ‘ expi-j ’ where $i \in \{50, 100, 200\}$ is the number of vertical levels and $j \in \{\text{rsup3}, \text{rsup5}, \text{weno5}\}$
 208 is the advective scheme combination.

An additional simulation, exp200-rsup5-smooth, is run with the rsup5 combination and a smoother bathymetry than in the baseline simulations. This choice is motivated by the result showing increased numerical mixing over steep topography. The hydrostatic consistency condition (sometimes called Haney number, Haney, 1991)) maximum value over the domain is ≈ 6 for exp200-rsup5-smooth and ≈ 17 for exp200-rsup5.

214 2.3 Online diagnostic of diapycnal diffusivity

We define the effective diapycnal mixing as the sum of the parameterized and the numerical (i.e., due to advection schemes) diapycnal mixing. Here we present how we diagnose the effective diapycnal diffusivity, called K_{eff} in this article, at each point in space and time during the model computation.

To do this, we first diagnose the temperature and salinity budgets, including all numerical sources of mixing. We use them to compute a buoyancy budget and in particular to isolate the non-advectional buoyancy fluxes. Finally, we project the fluxes in the direction orthogonal to the local isopycnal surfaces (based on local adiabatic density gradients) to obtain an effective diffusivity. The different steps are detailed below.

We first diagnose non-advectional tracer fluxes (\vec{F}^T, \vec{F}^S) for the potential temperature T and salinity S by closing the following budgets:

$$\frac{DT}{Dt} = \underbrace{T_t}_{T_{rate}} + \underbrace{\vec{u} \cdot \vec{\nabla} T}_{T_{adv}} = \underbrace{-\vec{\nabla} \cdot \vec{F}^T}_{T_{rhs}}$$

$$\frac{DS}{Dt} = \underbrace{S_t}_{S_{rate}} + \underbrace{\vec{u} \cdot \vec{\nabla} S}_{S_{adv}} = \underbrace{-\vec{\nabla} \cdot \vec{F}^S}_{S_{rhs}}$$

where the flux divergence on the r.h.s. includes contributions from: the parameterized vertical mixing from KPP, surface or bottom forcings, explicit horizontal mixing or implicit horizontal mixing due to the advection scheme (A. F. Shchepetkin & McWilliams, 2005), and other sources of numerical mixing such as implicit vertical advection (A. F. Shchepetkin, 2015), stabilisation of the isoneutral diffusive operator (Lemarié et al., 2012), or aspects related to the model time-stepping (A. Shchepetkin & McWilliams, 2008).

Non-advectional buoyancy fluxes are then computed by combining the tracer fluxes:

$$\vec{F}^B = -g(-\alpha \vec{F}^T + \beta \vec{F}^S)$$

where the thermal expansion coefficient $\alpha = -\frac{1}{\rho_0} \left(\frac{\partial \rho}{\partial T} \right)_S$ and the saline contraction coefficient $\beta = \frac{1}{\rho_0} \left(\frac{\partial \rho}{\partial S} \right)_T$ are computed using a local 3d linearization of the equation of state of the model (A. Shchepetkin & McWilliams, 2011).

Finally, to get an effective diapycnal diffusivity, we project the buoyancy fluxes (\vec{F}^B) in the direction orthogonal to the isopycnal surfaces $\vec{n} = \frac{\vec{\nabla} b}{|\vec{\nabla} b|}$ (where $\vec{\nabla} b$ are the adiabatic buoyancy gradients based on the definition of A. Shchepetkin and McWilliams (2011)) and divide by the norm of the same gradient:

$$K_{eff} = \vec{F}^B \cdot \frac{\vec{\nabla} b}{|\vec{\nabla} b|^2}$$

Table 1. List of experiments with their characteristic numerical features

Configuration name	Number of σ levels	Time step	Horizontal		Vertical		Horizontal		Vertical	
			advective scheme for momentum	advective scheme for momenta	advective scheme for active tracers	advective scheme for passive tracers	advective scheme for active tracers	advective scheme for passive tracers	advective scheme for active tracers	advective scheme for passive tracers
exp50-rsup3	50	80	up3	splines	rsup3	splines	rsup3	splines	rsup3	splines
exp100-rsup3	100	80	up3	splines	rsup3	splines	rsup3	splines	rsup3	splines
exp200-rsup3	200	80	up3	splines	rsup3	splines	rsup3	splines	rsup3	splines
exp50-rsup5	50	80	up3	splines	rsup5	splines	rsup5	splines	rsup5	splines
exp100-rsup5	100	80	up3	splines	rsup5	splines	rsup5	splines	rsup5	splines
exp200-rsup5	200	80	up3	splines	rsup5	splines	rsup5	splines	rsup5	splines
exp200-rsup5-smooth	200	80	up3	splines	rsup5	splines	rsup5	splines	rsup5	splines
exp50-weno5	50	80	up3	splines	rsup5	splines	rsup5	splines	rsup5	splines
exp100-weno5	100	80	up3	splines	rsup5	splines	rsup5	splines	rsup5	splines
exp200-weno5	200	80	up3	splines	rsup5	splines	rsup5	splines	rsup5	splines

In the (ideal) case where the mixing is dominated by the vertical mixing parameterization ($\vec{F}_B \approx (0, 0, K_{KPP} \frac{\partial b}{\partial z})$), and if we assume that the horizontal buoyancy gradients are small compared to the vertical stratification ($|\frac{\partial b}{\partial x}|, |\frac{\partial b}{\partial y}| \ll |\frac{\partial b}{\partial z}|$), we should recover: $K_{eff} = K_{KPP}$.

Note that the method has two obvious limitations. The first is that it is only valid as long as essentially dissipative advective schemes are used. Using a scheme dominated by dispersive errors without explicit diffusivity would lead to an underestimation of the effective diffusivity. In addition, the diffusivity K_{eff} will be ill-defined in regions where the stratification vanishes and the norm of the adiabatic buoyancy gradient goes to zero.

However, a strong advantage is that we do not need a passive tracer patch to estimate K_{eff} , which allows us to analyse effective mixing in parts of the domain that do not depend on the tracer patch spreading. In section 3.5, we use the estimation of the online effective mixing K_{eff} to study the impact of the topography on the effective mixing over areas not covered by tracer patches.

2.4 Diagnosis of diapycnal diffusivity based on tracer release experiments

Independent of the online diagnosis of effective mixing, we use TREs to diagnose the effective diffusivity in the model. In addition to providing a quantitative estimate of mixing, numerical TRE visually illustrate the diffusive and dispersive effects of the schemes.

Two passive tracers are released in each simulation. Tracer 1 is released over the abyssal plain in the Iceland Basin and tracer 2 is released over the Reykjanes Ridge. We expect the contrasting dynamics in these regions (smooth topography vs. rough topography) to produce different levels of mixing. The initial distributions of the tracer patches are Gaussian in density space:

$$c_{(t=0)} = \exp\left(-\frac{r^2}{2\sigma_r^2}\right) \exp\left(-\frac{(\rho - \rho_{target})^2}{2\sigma_\rho^2}\right)$$

, where $r = \sqrt{(x - x_C)^2 + (y - y_C)^2}$ and (x_C, y_C) is the location of the center of the patch, ρ_{target} is the initial target density, $\sigma_r = 2$ km, $\sigma_\rho = 0.01$ kg m⁻³. The initial location of the tracers was chosen to keep the tracer patches in the domain as long as possible. Figure 2 shows the release of the tracer 1 (panels a,e) and the tracer 2 (panels c,g) and how the tracer patches are distributed vertically and horizontally 15 days after the release (panels b,f and d,h).

Two different methods are used to diagnose the diapycnal diffusivity experienced by each tracer. There are presented in the following.

2.4.1 Taylor estimate of diffusivity

Taylor (1922) studied the evolution of a tracer with a concentration c that follows the equation $\frac{\partial c}{\partial t} = \kappa \nabla^2 c$, where κ is the turbulent diffusivity. The main result is that κ is related to the growth rate of the tracer concentration variance in the considered direction. To estimate the diapycnal diffusivity, oceanographers have considered the diapycnal direction. The estimated diffusivity K_{tr} can thus be written as:

$$K_{tr} = \frac{1}{2} \frac{1}{\langle |\nabla b|^2 \rangle} \frac{\partial}{\partial t} \langle (b - \langle b \rangle)^2 \rangle, \quad (2)$$

where b is buoyancy and $\langle \cdot \rangle$ is the tracer-weighted averaging operator:

$$\langle \cdot \rangle = \frac{\int \int \int c dx dy dz}{\int \int \int c dx dy dz}, \quad (3)$$

274 and the integral is taken over the full model volume.

275 For a constant mixing rate, we should recover $K_{tr} = \kappa$. Recently, Ruan and Fer-
276 rari (2021) revisited Taylor's theory in the general case where the mixing rate varies in
277 space. In this case, the interpretation of K_{tr} is more complicated. In the present sim-
278 ulations, KPP produces diapycnal mixing coefficients that rarely deviate from the back-
279 ground value in the ocean interior. We therefore expect K_{tr} to be as close as possible
280 to κ if no spurious numerical mixing has been produced.

281 2.4.2 A one-dimensional model of tracer spreading across isopycnals

282 We also use an alternative method to estimate the diapycnal diffusivity based on
283 a one-dimensional model describing the tracer evolution in buoyancy space. This model
284 has been widely used in field TREs (e.g., Ledwell & Watson, 1991) and in virtual TREs
285 (Holmes et al., 2019). It reads:

$$\frac{\partial \bar{c}}{\partial t} + \left(\bar{w} - \overline{\frac{\partial K_{fit}}{\partial h}} \right) \frac{\partial \bar{c}}{\partial h} = \overline{K_{fit}} \frac{\partial^2 \bar{c}}{\partial h^2}, \quad (4)$$

286 where w is the vertical velocity and the overbar denotes an average over buoyancy classes
287 at a given height h above the buoyancy class targeted at the tracer release. A mean strati-
288 fication profile is used to convert between h and b . The diapycnal diffusivity $\overline{K_{fit}}$ is as-
289 sumed to be a linear function of h , $\overline{K_{fit}} = \overline{K_0} + h \overline{\frac{\partial K_{fit}}{\partial h}}$, where K_0 is the diapycnal dif-
290 fusivity at the target buoyancy. We use the method and algorithm described in Appendix B
291 in Holmes et al. (2019) to infer K_{fit} . Briefly, Equation 4 is discretized and a least-square
292 method is used at each time step to find the three parameters $\overline{K_0}$, \overline{w} and $\overline{\frac{\partial K_{fit}}{\partial h}}$ that min-
293 imize the distance between the ‘observed’ \bar{c} inferred from the simulation and the 1-d model
294 prediction from the initial distribution.

295 3 Results

296 3.1 Overview of the simulated dynamics

297 We first present an overview of the dynamics in the region. The large-scale and mesoscale
298 dynamics are qualitatively similar in all simulations, and we only show examples from
299 only one simulation (exp200-rsup5).

300 Mesoscale currents are remarkably barotropic, with horizontal currents extending
301 from below the surface mixed layer to the seafloor (Figures 3a and 3b), as is character-
302 istic of high-latitude gyres (Le Corre et al., 2020). The vertical velocity (w) patterns have
303 smaller horizontal and vertical scales with large amplitudes throughout the whole wa-
304 ter column (Figure 3c). It is largely the signature of energetic internal waves, either gen-
305 erated by flow-topography interactions above the Reykjanes Ridge as internal tides or
306 lee waves or by the strong wind events in the gyre (Vic et al., 2021). The stratification,
307 represented by N^2 , is enhanced in the thermocline and decreases smoothly with depth
308 (Figure 3d). It is minimal in the surface and bottom mixed layers, with values eventu-
309 ally reaching zero and locally becoming negative. The vertical shear of horizontal veloc-
310 ity, S^2 , is enhanced in the thermocline and in the boundary layers (Figure 3e). Distinct
311 thin layers (≈ 100 m, a few vertical grid points) of elevated shear are characteristic of in-
312 ternal waves, especially near-inertial waves (Alford et al., 2016).

313 The Richardson number $Ri = S^2/N^2$ compares the destabilizing strength of shear
314 with the stabilizing effect of stratification. Regions of strong shear and weak stratifica-
315 tion are prone to shear instability and mixing, these regions correspond to values of Ri
316 less than the critical value Ri_c (Figure 3f). In the boundary layers we often have $Ri <$
317 Ri_c , while in the interior $Ri > Ri_c$ almost everywhere, except in some thin shear lay-
318 ers described above. Thus, in the interior, the resulting diffusivity coefficient computed

319 by KPP, K_{KPP} , is predominantly equal to its background value of $10^{-5} \text{ m}^2 \text{ s}^{-1}$ (Fig-
 320 ure 3g). In the boundary layers, K_{KPP} reaches high values up to $10^{-1} \text{ m}^2 \text{ s}^{-1}$ where con-
 321 vective instabilities occur.

322 To assess the realism of the parametrised mixing coefficients K_{KPP} , we compared
 323 them with microstructure estimates from three cruises: OVIDE08 (Ferron et al., 2014),
 324 RREX15 (Branellec & Thierry, 2016), and RREX17 (Branellec & Thierry, 2018). Microstructure-
 325 based estimates are computed following Osborn (1980):

$$\kappa = \Gamma \frac{\epsilon}{N^2} \quad (5)$$

326 where $\Gamma = 0.2$ is the mixing efficiency, ϵ is the turbulent energy dissipation and N^2 is
 327 the stratification. Both ϵ and N^2 are estimated from probes mounted on a vertical mi-
 328 crostructure profiler (instrument manufactured by Rockland Scientific International Inc.).
 329 Details of the processing can be found in Ferron et al. (2014). The three cruises sam-
 330 pled the same section across the Reykjanes Ridge (shown in Figure 1). All products are
 331 shown in Figure 4. Data are binned on the same vertical grid with 100 m bins to facil-
 332 itate comparison. The in situ estimates all show contrasting profiles between the Reyk-
 333 janes Ridge and the Iceland Basin. Over the ridge, mixing increases from below the ther-
 334 mocline ($10^{-5} \text{ m}^2 \text{ s}^{-1}$) down to the bottom ($10^{-4} \text{ m}^2 \text{ s}^{-1}$), which is typical of internal
 335 tide-driven mixing over mid-ocean ridges (Waterhouse et al., 2014). Over the abyssal plain
 336 in the Iceland Basin, mixing is reduced and is close to $10^{-5} \text{ m}^2 \text{ s}^{-1}$ throughout the whole
 337 water column. Overall, K_{KPP} is close to κ in the ocean interior and off the ridge, but
 338 is smaller over the ridge in the ≈ 1000 m above the seafloor. The model likely misses some
 339 intensified mixing events associated with internal wave breaking over rough topography
 340 and does not generate enough vertical shear to reach low enough Richardson numbers.
 341 The effective mixing K_{eff} is close to the KPP mixing (and observations) off the ridge.
 342 But it is higher than the KPP mixing over the ridge (fig. 4a)), highlighting the presence
 343 of numerical mixing over topographic slopes, in regions showing increased in-situ diffu-
 344 sivities.

345 3.2 Parameterized vs effective mixing

346 Overall, the effective diffusivity K_{eff} is close to K_{KPP} (Figure 3h). However, it
 347 is significantly larger in areas located above the steepest slopes of the seafloor topogra-
 348 phy above the Reykjanes Ridge, over a depth extending from the seafloor to several hun-
 349 dred meters or more above. We quantified this discrepancy more systematically by com-
 350 puting some statistics of K_{eff} in two contrasting regions, above the ridge and above the
 351 abyssal plain of the Iceland Basin, for the simulations with 50, 100 and 200 levels (Fig-
 352 ure 5). Overall, it confirms the impression that K_{eff} departs from K_{KPP} above the ridge
 353 in the lowermost 1000 m above the seafloor ($10^{-4} \text{ m}^2 \text{ s}^{-1}$ vs $10^{-5} \text{ m}^2 \text{ s}^{-1}$), but is close
 354 to K_{KPP} in the abyssal plain.

355 Above the abyssal plain, increasing the number of σ -levels slightly reduces the ef-
 356 fective mixing. This is especially true when increasing the number of levels from 50 to
 357 100. There is also a slight improvement when increasing the number of levels from 100
 358 to 200, as effective and parameterized mixing become very comparable. However, there
 359 are differences between effective and parameterized mixing above the ridge, regardless
 360 of the resolution. Furthermore, the differences are not significantly reduced when increas-
 361 ing the number of levels from 100 to 200, and even increase in the lower 800 m.

362 The intensification of K_{eff} with increasing vertical resolution above the ridge is
 363 counterintuitive. In fact, this intensification is related to numerical constraints on the
 364 isoneutral rotation of the diffusive part of the RSUP3/5 operators (Lemarié et al., 2012).
 365 These limits consist of conditions on the maximum isopycnal slope α_m and the maxi-
 366 mum grid slope ratio s_m for which the diffusive part of the advection schemes can be ro-

367 tated along isopycnals:

$$\alpha_m = \max \left(\frac{\partial \rho}{\partial x} / \frac{\partial \rho}{\partial z}, \frac{\partial \rho}{\partial y} / \frac{\partial \rho}{\partial z} \right) < \alpha_c = 0.05 \quad (6)$$

$$s_m = \max \left(\frac{|\Delta_x \rho|}{|\Delta_z \rho|}, \frac{|\Delta_y \rho|}{|\Delta_z \rho|} \right) < s_c = 1, \quad (7)$$

368 where Δ_i represents the difference between neighboring grid points in the i direction.
 369 If $\alpha_m > \alpha_c$ or $s_m > s_c$, the diffusion will be along a direction that is not strictly aligned
 370 with isopycnals. This results in spurious diapycnal diffusion. Figures 6d and 6e show s_m ,
 371 and Figures 6g and 6h show α_m in simulations exp50-rsup5 and exp200-rsup5. There
 372 is a clear contrast between the abyssal plain, where $s_m < s_c$ and $\alpha_m < \alpha_c$, and the
 373 ridge, which has large areas with $s_m > s_c$ and $\alpha_m > \alpha_c$. Two reasons can be given
 374 to explain these differences. First, the ridge seafloor topography has larger gradients, hence
 375 the larger grid aspect ratio throughout the water column. Second, the enhanced inter-
 376 nal wave activity over the ridge means that isopycnal slopes may be locally steeper than
 377 in the rest of the domain. Overall, the grid points that do not satisfy Equations 6 or 7
 378 are associated with enhanced K_{eff} (Figure 6). Also, while increasing the number of ver-
 379 tical levels does not qualitatively change the isopycnal slope (Figure 6g vs Figure 6h),
 380 it changes the grid slope ratio (Figure 6d vs Figure 6e), which has the direct effect of fur-
 381 ther increasing K_{eff} (Figure 6a vs Figure 6b). This is also noticeable along the tracer
 382 path (Figure 11).

383 Another interesting feature that emerges from increasing the number of levels is
 384 the sharpening of the contrast between interior and boundary mixing. The bottom bound-
 385 ary layer is better defined in the 100-level and 200-level simulations than in the 50-level
 386 simulation. This is likely to have important implications for water mass transformation
 387 near the bottom (Baker et al., 2023).

388 Quantitatively, we also find that the effective mixing converges at 100 σ -levels above
 389 the ridge, but not above the abyssal plain. At a depth of 1500 meters, 100 σ -levels cor-
 390 respond to a vertical resolution of ≈ 25 meters above the ridge and ≈ 50 meters above
 391 the abyssal plain (see fig. Appendix Ab)). When 200 σ -levels are used, the vertical res-
 392 olution at 1500 meters depth reaches ≈ 25 meters also above the abyssal plain (see fig.
 393 Appendix Ac)). This is also an important factor that will make a difference in the spread-
 394 ing of the tracer patches.

395 3.3 Spreading of the passive tracers

396 We now examine what happens to the 2 passive tracers released in the simulation
 397 in the abyssal plain and above the ridge.

398 The tracer concentration 10 days after release for the tracer released over the abyssal
 399 plain (tracer 1) is shown in Figure 7 for the different simulations. The most striking fea-
 400 ture is the dispersive patterns obtained at the lowest vertical resolution (50 levels) when
 401 using the upstream horizontal advection schemes (rsup3 and rsup5) in combination with
 402 the vertical advection scheme splines. This dispersion is associated with the hyperdif-
 403 fusivity (Boyd, 1994; Jiménez, 1994). It is strongly reduced by doubling the number of
 404 vertical levels to 100, and further reduced with 200 levels. The weno5 scheme combina-
 405 tion is more diffusive, and the difference is most significant with 50 levels. Increasing the
 406 number of levels to 100 or 200 levels significantly improves the tracer representation by
 407 reducing numerical diffusion.

408 The tracer concentration for the tracer released above the ridge (tracer 2) is shown
 409 in Figure 8. Overall, the two tracers show the same characteristics with respect to the
 410 advection schemes used. Importantly, the differences between the combinations of schemes

411 are most pronounced when 50 levels are used, and gradually disappear when 100 and 200
 412 levels are used. The results in all cases seem to converge between 100 and 200 levels.

413 3.4 Numerical mixing above the abyssal plain

414 We now compare the parameterized diffusivity in the model (K_{KPP}) with our dif-
 415 ferent estimates for the diapycnal diffusivity: the effective diffusivity K_{eff} based on the
 416 online buoyancy budget and the tracer-based diapycnal diffusivities K_{fit} and K_{tr} diag-
 417 nosed from the tracer spreading across isopycnals (Section 2.4).

418 These different estimates are shown in Fig. 9 for tracer 1, released above the abyssal
 419 plain. K_{KPP} and K_{eff} are weighted by the tracer concentration and can thus be inter-
 420 preted as the average diffusivity coefficients seen by the tracer. Thus, while K_{KPP} should
 421 represent the diffusivity experienced by the tracer in the absence of additional diffusiv-
 422 ity due to the advection schemes, K_{eff} represents the actual, effective mixing, which is
 423 the sum of the prescribed mixing (from KPP) and the numerical mixing due to the ad-
 424 vection schemes. The four estimates are diagnosed for each time step over the first 15
 425 days after tracer release, and box plots represent their distribution over this period.

426 Basically, K_{KPP} and K_{eff} are close to $10^{-5} \text{ m}^2 \text{ s}^{-1}$ (background mixing in KPP)
 427 in all simulations, regardless of the number of vertical levels and the combination of schemes.
 428 This background value can be seen as the modeler's target diffusivity, which the mod-
 429 er wants to be as close as possible to the parameterized value.

430 The two tracer-based estimates show large differences with the effective and pa-
 431 rameterized diffusivities at the coarser vertical resolution, with diffusivities up to two or-
 432 ders of magnitude larger (comparable to what is seen in bracco2018, for example). Us-
 433 ing 50 vertical levels, both tracers experienced large diffusivities, two orders of magni-
 434 tude larger than the parameterized diffusivities. However, increasing the number of ver-
 435 tical levels significantly reduces the mixing experienced by the tracers. Overall, doubling
 436 the number of vertical levels from 50 to 100 reduces the diffusivity experienced by tracer 1
 437 by an order of magnitude, and again when doubling from 100 to 200. This is true for all
 438 the advection schemes used. With 50 levels, K_{tr} reaches median values of $1-3 \times 10^{-3} \text{ m}^2 \text{ s}^{-1}$,
 439 which are two orders of magnitude larger than the targeted diffusivity. With 200 levels,
 440 K_{tr} is reduced to $1 - 4 \times 10^{-5} \text{ m}^2 \text{ s}^{-1}$, much closer to the parameterized values.

441 For the same vertical resolution, the weno5 combination is on average 2-3 times more
 442 diffusive than the rsup3 and rsup5 combinations. Even with 200 levels, the two tracer-
 443 based estimates do not converge to the effective mixing diagnosed in the simulation. The
 444 differences between rsup3 and rsup5 are small, although K_{tr} is slightly larger for rsup5.
 445 While the dissipative part of the advection scheme is expected to be about two times smaller
 446 for rsup5 (visible in the slightly smaller effective diffusivities), the dispersive effects are
 447 stronger for the 5-th order scheme, leading to slightly larger tracer-based diffusivities.

448 Note that K_{fit} , which is expected to be comparable to K_{tr} , is much smaller for the
 449 50- and 100-level simulations using rsup3 and rsup5. We attribute this discrepancy to
 450 a limit of the 1-d fit method when using a coarse vertical grid resolution in the presence
 451 of dispersive errors. Indeed, the 1-d distribution of the tracer in buoyancy space does
 452 not smoothly fit a Gaussian distribution (Figure 10), a requirement for the method to
 453 be reliable (Holmes et al., 2019). The difference between K_{tr} and K_{fit} is much smaller
 454 for exp50-weno5, which uses a more diffusive scheme. The difference between K_{tr} and
 455 K_{fit} disappears for exp200-rsup3 and exp200-rsup5. This confirms the visual impres-
 456 sion in Figure 7 that the dispersive effect of the upstream/splines combination disappears
 457 with 200 levels.

458 Naively, we might have expected K_{tr} (and to lesser extent, K_{fit}) to be closer to
 459 K_{eff} for the rsup3 and rsup5 simulations even with 50 and 100 levels. Indeed, these sim-

ulations use the same advection schemes for the active tracers, used to diagnose K_{eff} , and for the passive tracers. However, the initial gradients of the passive tracers are much larger than the temperature and salinity gradients at comparable depths. This leads to increased dispersion of the passive tracers, which ultimately leads to increased tracer variance in buoyancy space, hence the larger values of K_{tr} as compared to K_{eff} .

465 3.5 Numerical mixing above the ridge

466 Tracer 2 is released above the ridge, where we expect higher levels of numerical mixing
 467 in the model, as seen in section . The tracer-weighted parameterised mixing K_{KPP}
 468 (Fig.) is not much different than above the abyssal plain, and remains close to the back-
 469 ground value ($10^{-5} \text{ m}^2 \text{ s}^{-1}$), showing that tracer 2 does not enter the bottom bound-
 470 ary layer. However, the effective mixing seen by tracer 2, K_{eff} , departs from K_{KPP} by
 471 a factor of 2-3 for the 50-level simulations and by an order of magnitude for the 200-level
 472 simulations. This enhancement is due to the slope limiters (see section) and is confined
 473 to above the ridge as shown in Figures 6a and 6b.

474 Similar conclusions as for tracer 1 can be drawn for the tracer-based diapycnal dif-
 475 fusivities estimated for tracer 2. Specifically, for a given set of advection schemes, increas-
 476 ing the vertical resolution reduces the tracer-based diffusivity (Figure 11) until it reaches
 477 the effective mixing values. Using 50 levels is still too coarse for the fit method, and K_{fit}
 478 is much smaller than K_{tr} . However, with 100 and 200 levels, there is good agreement
 479 between K_{fit} and K_{tr} , which gives us confidence in the relevance of using TREs to di-
 480 agnose mixing.

481 Among the different sets of schemes used, the weno5 combination is still more dif-
 482 fusive by a factor of 2 to 5 (depending on the vertical resolution) compared to rsup3 and
 483 rsup5. Among the upstream biased schemes, rsup5 is slightly less diffusive than rsup3,
 484 as expected.

485 3.6 Effect of smoothing topography

486 Since the largest numerical mixing occurs over the steepest topographic slopes, it
 487 is tempting to further smooth the original topography in order to reduce numerical mix-
 488 ing. We tested this workaround by using a smoothing Gaussian kernel with three times
 489 the characteristic scale. We used this smoothed topography to run simulation exp200-
 490 rsup5-smooth, based on exp200-rsup5, which is the simulation that produces the least
 491 numerical mixing. Figure 12a,b,c shows the baseline bathymetry, the smoothed bathymetry,
 492 and the difference between the two. The difference in the distribution of topographic slopes
 493 between the baseline topography and the modified topography is shown in Figure 12d).
 494 While the baseline topography contains a non-negligible number of grid points with slopes
 495 greater than 10% and up to 20%, the modified topography has slopes limited to 11% and
 496 only a handful of slopes greater than 10%. Visually, the large-scale topographic struc-
 497 tures of the ridge are preserved (Figure 6b vs 6c).

498 The effect of increasing the smoothing can be seen directly in α_m and s_m , which
 499 are reduced over the steepest slopes of the ridge (Figures 6f and 6i). The fraction of grid
 500 points with $\alpha_m > \alpha_c$ and $s_m > s_c$ is significantly reduced. As a result, K_{eff} decreases
 501 and is much closer to the parameterised background value (Figure 6c).

502 The efficiency of smoothing the topography to reduce numerical mixing is well il-
 503 lustrated and quantified by the TRE of tracer 2 released over the ridge (Figure 13). In
 504 short, K_{eff} , K_{fit} and K_{tr} are all reduced by an order of magnitude and converge to K_{KPP} .
 505 Note that there is a physical effect of smoothing the topography that adds to the nu-
 506 matical effect, which is to reduce the energetic turbulence associated with flow-topography
 507 interactions and, in particular, the generation of internal tides. Thus, the isopycnal slopes
 508 above the ridge are reduced, which helps to reduce α_m .

509 **4 Summary and Discussion**

510 In this study, we investigated the diapycnal mixing in a realistic high-resolution sim-
 511 ulation using a terrain-following coordinate model (CROCO) in a regional domain over
 512 the Reykjanes Ridge, including tides and high-frequency winds. In particular, we tested
 513 the impact of some numerical choices, namely, the advection schemes and the vertical
 514 resolution, on the amount of "spurious" numerical diapycnal mixing in the interior of
 515 the ocean. We implemented two types of diagnostics to estimate the effective diapycnal
 516 mixing in the simulations, defined as the sum of the parameterized mixing and the nu-
 517 merical mixing. First, we implemented an online diagnostic, based on the computation
 518 of buoyancy fluxes across isopycnal surfaces at each time step of the model. In par-
 519 allel, we tested an alternative and complementary method based on TREs (Holmes et al.,
 520 2019; Ruan & Ferrari, 2021).

521 We used 10 configurations that differ in the horizontal and vertical advection schemes
 522 used and the number of vertical levels (Table 1). The results can be summarized as fol-
 523 lows:

- 524 • Using standard numerical parameters for a submesoscale-permitting simulation
 525 ($\Delta x = 800$ m) over the Reykjanes Ridge, the dynamics do not generate signifi-
 526 cant mixing in the interior by the KPP scheme, despite the intense internal wave
 527 activity. Vertical shear, mostly driven by internal waves, remains too small to trig-
 528 ger Richardson-based mixing. Therefore, the parameterized mixing is close to its
 529 background value in the interior over most of the domain and slightly weaker than
 530 the observed mixing. The parameterization fails to reproduce the contrast between
 531 ridge and abyssal with intensified mixing in the lowest part of the water column
 532 above the ridge. Nonetheless, the effective mixing is enhanced above the ridge, which
 533 has a steeper seafloor topography. This led us to study these two regions separately.
- 534 • Over the abyssal plain, the effective mixing is close to the parameterized mixing,
 535 i.e. there is no significant numerical mixing despite the presence of internal waves,
 536 thanks to the isoneutral diffusive operator used for active tracers in the model.
 537 However, over the ridge, in the presence of steeper slopes, the effective mixing is
 538 an order of magnitude larger than the parameterized mixing when using standard
 539 numerical parameters and topography treatment. This difference is explained by
 540 the presence of steep slopes, and in particular a grid slope ratio (also called hy-
 541 drostatic inconsistency number) larger than 1, which limits the efficiency of the
 542 isoneutral diffusive operator.
- 543 • The numerical mixing can be greatly reduced by additional smoothing of the to-
 544 pography to ensure values of the grid slope ratio less than 1. In this case, the ef-
 545 fective mixing is very close to the parameterized mixing over the entire domain.
- 546 • The tracer-based diffusivity estimates are much larger than the effective and pa-
 547 rameterized mixing of the model at low vertical resolutions. Using 50 levels, the
 548 tracer-based diffusivities are two orders of magnitude larger than the effective mix-
 549 ing (10^{-3} m² s⁻¹ vs 10^{-5} m² s⁻¹). This is explained either by dispersive effects
 550 in the vertical advection of the tracers when using a combination of RSUP3/5 in
 551 the horizontal and SPLINES in the vertical, or by strong diffusive effects when us-
 552 ing WENO5 schemes in the horizontal and vertical. Using 100 levels greatly re-
 553 duces these effects and reduces tracer-based diffusivities by an order of magnitude.
 554 When 200 levels are used, the tracer-based diffusivity is further reduced, and con-
 555 verges to the effective diffusivity. We also find that WENO5 schemes are on av-
 556 erage two to three times more diffusive than the combinations of RSUP3/5 in the
 557 horizontal and SPLINES in the vertical, regardless of the number of levels.

558 Reducing, or at least controlling, numerical mixing in global and regional ocean mod-
 559 els has been a major concern of the community (e.g., Griffies et al., 2000; Burchard &
 560 Rennau, 2008; Marchesiello et al., 2009; Hill et al., 2012). Our study shows that it nec-

561 necessarily involves dilemmas. While increasing the vertical resolution actually reduces dispersive and/or diffusive effects of advective schemes and leads to a more realistic representation of tracers, it also increases numerical mixing through increasing the grid slope ratio beyond acceptable limits, which renders the isoneutral diffusive operator less effective.

566 Thus, if limiting the numerical mixing to values less than the parameterized mixing in the interior of the ocean is a priority, e.g. when performing a long-term equilibration or studying water mass transformation, one must be very careful in controlling the numerical mixing. An obvious solution is to further smooth the topography to ensure that the grid slope ratio remains below one most of the time. This is largely achieved by keeping the hydrostatic consistency condition near unity. But the downside is that this would also change the flow-topography interactions, since small-scale topographic features are important for converting barotropic tides into high-mode internal waves (de Lavergne et al., 2020) or for generating submesoscale instabilities (Gula et al., 2016). A promising solution to these problems might be the Brinkman penalization approach (Debreu et al., 2020, 2022), which allows to account for steep topographic slopes without increasing the grid slope ratio excessively.

578 A time filter can be added to the isoneutral slope calculation to limit possible numerical instabilities due to the nonlinearity of the equation of state in certain regimes (Griffies et al., 1998). This was not used in the experiments presented here, and no evidence of numerical instabilities related to isoneutral diffusion was found. However, we performed an additional experiment using exponential time smoothing with a time scale of 1 day (the default value in CROCO), which is shown in the appendix Appendix C. Even with a time scale as small as 1 day, it still leads to a noticeable increase in the numerical diffusivity due to the presence of high-frequency processes and fast isopycnal oscillations, as is the case here.

587 Appendix A Grid resolution

588 Figure A1 shows the vertical resolution at a section in the center of the grid. Note
589 that the vertical resolution depends on the number of terrain-following levels.

590 Appendix B Use of monotone advective schemes to limit negative tracer 591 concentration

592 Here we show the histogramm of tracer 1 concentration over 40 days of simulation
593 using 50 σ -levels and combination of advective scheme r³, r⁵ and weno5. We see
594 that there is almost no negative values for the concentration of tracer 1 when the com-
595 bination of advective weno5 is applied.

596 Appendix C Test with a isoneutral slope temporal filter and a cen- 597 tered advective scheme (C4)

598 Here we present some additional tests that we performed. We compare the exp100-
599 r³ configuration presented above with two additional configurations:

- 600 • exp100-r³-filt, which is the same configuration as exp100-r³ with an addi-
601 tional temporal filter that modifies the isoneutral slopes. This filter is activated
602 by the "TS_MIX_ISO_FILT" key in CROCO. It is an exponential smoothing with
603 a time scale of 1 day;
- 604 • exp100-c4, which uses a fourth-order centered advective scheme (C4) for the hor-
605 izontal advection of the tracers, with no additional diffusivity added. The rest of
606 the configuration is identical to exp100-r³.

Using the time filter, we see that the effective mixing increases by a factor of 3 to 5 over the abyssal plain and the ridge (Fig. C1). The 1-day time scale is large enough to suppress isopycnal oscillations due to high-frequency processes. We also tested a time scale of 3 hours (not shown) and still observed an increase in effective diffusivity compared to the case with no time filtering.

The use of a centered advective scheme for tracer advection without diffusivity would be considered a bad numerical practice, as it is expected to lead to strong dispersive errors. And this is exactly what we observe here. The tracer-based diffusivities are much higher for both tracers than for any other configuration, leading to a much larger dispersion of the tracer cloud and extra diapycnal diffusivities. Above the abyssal plain, the effective diffusivity is very small because the method does not allow for dispersive effects. Above the ridge, the effective mixing is stronger in exp100-c4 compared to exp100-rsup3 only because the tracer penetrates inside the lower boundary layer.

Appendix D Open Research

AGU requires an Availability Statement for the underlying data needed to understand, evaluate, and build upon the reported research at the time of peer review and publication.

Authors should include an Availability Statement for the software that has a significant impact on the research. Details and templates are in the Availability Statement section of the Data and Software for Authors Guidance: <https://www.agu.org/Publish-with-AGU/Publish/Author-Resources/Data-and-Software-for-Authors#availability>

It is important to cite individual datasets in this section and, and they must be included in your bibliography. Please use the type field in your bibtex file to specify the type of data cited. Some options include Dataset, Software, Collection, Computation-alNotebook. Ex:

```
632
633 @misc{https://doi.org/10.7283/633e-1497,
634   doi = {10.7283/633E-1497},
635   url = {https://www.unavco.org/data/doi/10.7283/633E-1497},
636   author = {de Zeeuw-van Dalfsen, Elske and Sleeman, Reinoud},
637   title = {KNMI Dutch Antilles GPS Network - SAB1-St_Johns_Saba_NA P.S.},
638   publisher = {UNAVCO, Inc.},
639   year = {2019},
640   type = {dataset}
641 }
642
```

For physical samples, use the IGSN persistent identifier, see the International Geo Sample Numbers section: <https://www.agu.org/Publish-with-AGU/Publish/Author-Resources/Data-and-Software-for-Authors#IGSN>

Acknowledgments

The authors would like to acknowledge Bruno Ferron for the in-situ data from campaigns RREX15, RREX17 and OVIDE08. We also would like to acknowledge Ryan Holmes for sharing his code to compute the diffusivities K_{fit} . This work was supported by the French National Agency for Research (ANR) through the project DEEPER (ANR-19-CE01-0002-01), by the Office of Naval Research (ONR grant N00014-23-1-2226), and by ISblue project, Interdisciplinary graduate school for the blue planet (ANR-17-EURE-0015) and co-funded by a grant from the French government under the program "Investissements d'Avenir"

654 embedded in France 2030. Simulations were performed using HPC resources from GENCI-
 655 TGCC (Grants 2022-A0090112051), and from HPC facilities DATARMOR of “Pôle de
 656 Calcul Intensif pour la Mer” at Ifremer Brest France.

657 References

- 658 Alford, M. H. (2020). Global calculations of local and remote near-inertial-wave dis-
 659 sipation. *Journal of Physical Oceanography*, 50(11), 3157–3164. doi: 10.1175/
 660 JPO-D-20-0106.1
- 661 Alford, M. H., MacKinnon, J. A., Simmons, H. L., & Nash, J. D. (2016). Near-
 662 inertial internal gravity waves in the ocean. *Annu. Rev. Mar. Sci.*, 8, 95–123.
 663 doi: 10.1146/annurev-marine-010814-015746
- 664 Arbic, B. K. (2022). Incorporating tides and internal gravity waves within global
 665 ocean general circulation models: A review. *Progress in Oceanography*, 102824.
 666 doi: 10.1016/j.pocean.2022.102824
- 667 Arbic, B. K., Wallcraft, A. J., & Metzger, E. J. (2010). Concurrent simulation of
 668 the eddying general circulation and tides in a global ocean model. *Ocean Mod-
 669 elling*, 32(3-4), 175–187. doi: 10.1016/j.ocemod.2010.01.007
- 670 Auclair, F., Benshila, R., Bordois, L., Boutet, M., Brémont, M., Caillaud, M., ...
 671 Theetten, S. (2022, December). *Coastal and regional ocean community model*.
 672 Zenodo. Retrieved from <https://doi.org/10.5281/zenodo.7415343> doi:
 673 10.5281/zenodo.7415343
- 674 Baker, L., Mashayek, A., & Naveira Garabato, A. (2023). Boundary upwelling of
 675 Antarctic Bottom Water by topographic turbulence. *AGU Advances*, 4(5),
 676 e2022AV000858. doi: 10.1029/2022AV000858
- 677 Beckmann, A., & Haidvogel, D. B. (1993). Numerical simulation of flow around a
 678 tall isolated seamount. part i: Problem formulation and model accuracy. *Jour-
 679 nal of Physical Oceanography*, 23(8), 1736–1753.
- 680 Boyd, J. P. (1994). Hyperviscous shock layers and diffusion zones: Monotonicity,
 681 spectral viscosity, and pseudospectral methods for very high order differential
 682 equations. *Journal of Scientific Computing*, 9(1), 81–106. Retrieved from
 683 <https://doi.org/10.1007/BF01573179> doi: 10.1007/BF01573179
- 684 Bracco, A., Choi, J., Kurian, J., & Chang, P. (2018). Vertical and horizontal reso-
 685 lution dependency in the model representation of tracer dispersion along the
 686 continental slope in the northern gulf of mexico. *Ocean Modelling*, 122, 13–25.
 687 doi: <https://doi.org/10.1016/j.ocemod.2017.12.008>
- 688 Branellec, P., & Thierry, V. (2016). Rrex 2015. ctd-o2 data report.
- 689 Branellec, P., & Thierry, V. (2018). *Rrex 2017. ctd-o2 data report, rap. int* (Tech.
 690 Rep.). LOPS/18-04, <https://doi.org/10.13155/58074>.
- 691 Burchard, H., & Rennau, H. (2008). Comparative quantification of physically and
 692 numerically induced mixing in ocean models. *Ocean Modelling*, 20(3), 293–311.
 693 doi: 10.1016/j.ocemod.2007.10.003
- 694 Debreu, L., Kevlahan, N.-R., & Marchesiello, P. (2020). Brinkman volume penaliza-
 695 tion for bathymetry in three-dimensional ocean models. *Ocean Modelling*, 145,
 696 101530. Retrieved from <https://www.sciencedirect.com/science/article/pii/S146350031930174X> doi: <https://doi.org/10.1016/j.ocemod.2019.101530>
- 697 Debreu, L., Kevlahan, N.-R., & Marchesiello, P. (2022). Improved gulf stream
 698 separation through brinkman penalization. *Ocean Modelling*, 179, 102121.
 699 Retrieved from <https://www.sciencedirect.com/science/article/pii/S1463500322001354> doi: <https://doi.org/10.1016/j.ocemod.2022.102121>
- 700 de Lavergne, C., Falahat, S., Madec, G., Roquet, F., Nylander, J., & Vic, C. (2019).
 701 Toward global maps of internal tide energy sinks. *Ocean Modell.*, 137, 52–75.
 702 doi: 10.1016/j.ocemod.2019.03.010
- 703 de Lavergne, C., Groeskamp, S., Zika, J., & Johnson, H. L. (2022). The role of mix-
 704 ing in the large-scale ocean circulation. In *Ocean mixing* (pp. 35–63). Elsevier.
- 705

- 707 doi: <https://doi.org/10.1016/B978-0-12-821512-8.00010-4>
- 708 de Lavergne, C., Vic, C., Madec, G., Roquet, F., Waterhouse, A., Whalen, C.,
 709 ... Hibiya, T. (2020). A parameterization of local and remote tidal
 710 mixing. *Journal of Advances in Modeling Earth Systems*, 12(5). doi:
 711 10.1029/2020MS002065
- 712 Furon, B., Kokoszka, F., Mercier, H., & Lherminier, P. (2014). Dissipation rate
 713 estimates from microstructure and finescale internal wave observations along
 714 the A25 Greenland–Portugal OVIDE line. *Journal of Atmospheric and Oceanic
 715 Technology*, 31(11), 2530–2543.
- 716 Frajka-Williams, E., Brearley, J. A., Nash, J. D., & Whalen, C. B. (2022). New tech-
 717 nological frontiers in ocean mixing. In *Ocean mixing* (pp. 345–361). Elsevier.
- 718 Griffies, S. M., Gnanadesikan, A., Pacanowski, R. C., Larichev, V. D., Dukow-
 719 icz, J. K., & Smith, R. D. (1998). Isoneutral diffusion in a z-coordinate
 720 ocean model. *Journal of Physical Oceanography*, 28(5), 805 - 830. Retrieved
 721 from https://journals.ametsoc.org/view/journals/phoc/28/5/1520-0485_1998_028_0805_idiazc_2.0.co_2.xml doi: 10.1175/1520-0485(1998)028<0805:IDIAZC>2.0.CO;2
- 722 Griffies, S. M., Pacanowski, R. C., & Hallberg, R. W. (2000). Spurious di-
 723 apycnal mixing associated with advection in a z-coordinate ocean model.
Monthly Weather Review, 128(3), 538–564. doi: [https://doi.org/10.1175/1520-0493\(2000\)128<0538:SDMAWA>2.0.CO;2](https://doi.org/10.1175/1520-0493(2000)128<0538:SDMAWA>2.0.CO;2)
- 724 Gula, J., Blacic, T. M., & Todd, R. E. (2019). Submesoscale coherent vortices in the
 725 Gulf Stream. *Geophysical Research Letters*, 46(5), 2704–2714. doi: 10.1029/2019GL081919
- 726 Gula, J., Molemaker, M. J., & McWilliams, J. C. (2016). Topographic generation of
 727 submesoscale centrifugal instability and energy dissipation. *Nat. Commun.*, 7.
 728 doi: 10.1038/ncomms12811
- 729 Gula, J., Theetten, S., Cambon, G., & Roullet, G. (2021, June). *Description of the
 730 gigatl simulations*. Zenodo. Retrieved from <https://doi.org/10.5281/zenodo.4948523> doi: 10.5281/zenodo.4948523
- 731 Haney, R. L. (1991). On the pressure gradient force over steep topography
 732 in sigma coordinate ocean models. *Journal of Physical Oceanography*,
 733 21(4), 610 - 619. Retrieved from https://journals.ametsoc.org/view/journals/phoc/21/4/1520-0485_1991_021_0610_otpgfo_2.0.co_2.xml doi:
 734 10.1175/1520-0485(1991)021<0610:OTPGFO>2.0.CO;2
- 735 Hecht, M. W. (2010). Cautionary tales of persistent accumulation of numerical error:
 736 Dispersive centered advection. *Ocean Modelling*, 35(3), 270–276. doi: 10.1016/j.ocemod.2010.07.005
- 737 Hill, C., Ferreira, D., Campin, J.-M., Marshall, J., Abernathey, R., & Barrier, N.
 738 (2012). Controlling spurious diapycnal mixing in eddy-resolving height-
 739 coordinate ocean models—insights from virtual deliberate tracer release ex-
 740 periments. *Ocean Modelling*, 45, 14–26. doi: 10.1016/j.ocemod.2011.12.001
- 741 Hofmann, M., & Morales Maqueda, M. (2006). Performance of a second-order
 742 moments advection scheme in an ocean general circulation model. *Journal
 743 of Geophysical Research: Oceans*, 111(C5). doi: <https://doi.org/10.1029/2005JC003279>
- 744 Holmes, R. M., de Lavergne, C., & McDougall, T. J. (2019). Tracer transport within
 745 abyssal mixing layers. *Journal of Physical Oceanography*, 49(10), 2669–2695.
 746 doi: <https://doi.org/10.1175/JPO-D-19-0006.1>
- 747 Jayne, S. R., & St Laurent, L. C. (2001). Parameterizing tidal dissipation over
 748 rough topography. *Geophysical Research Letters*, 28(5), 811–814. doi: 10.1029/2000GL012044
- 749 Jiang, G.-S., & Shu, C.-W. (1996). Efficient implementation of weighted
 750 eno schemes. *Journal of Computational Physics*, 126(1), 202-228. Retrieved
 751 from <https://www.sciencedirect.com/science/article/pii/>

- 762 S0021999196901308 doi: <https://doi.org/10.1006/jcph.1996.0130>
- 763 Jiménez, J. (1994). Hyperviscous vortices. *Journal of Fluid Mechanics*, 279,
764 169–176. doi: 10.1017/S0022112094003861
- 765 Kunze, E., Firing, E., Hummon, J. M., Chereskin, T. K., & Thurnherr, A. M.
766 (2006). Global abyssal mixing inferred from lowered adcp shear and ctd
767 strain profiles. *Journal of Physical Oceanography*, 36(8), 1553–1576. doi:
768 <https://doi.org/10.1175/JPO2926.1>
- 769 Large, W. G., McWilliams, J. C., & Doney, S. C. (1994). Oceanic vertical mixing: A
770 review and a model with a nonlocal boundary layer parameterization. *Reviews
771 of geophysics*, 32(4), 363–403. doi: <https://doi.org/10.1029/94RG01872>
- 772 Le Corre, M., Gula, J., & Tréguier, A.-M. (2020). Barotropic vorticity balance of
773 the North Atlantic subpolar gyre in an eddy-resolving model. *Ocean Science*,
774 16(2), 451–468. doi: 10.5194/os-16-451-2020
- 775 Ledwell, J. R., Montgomery, E., Polzin, K., St Laurent, L., Schmitt, R., & Toole, J.
776 (2000). Evidence for enhanced mixing over rough topography in the abyssal
777 ocean. *Nature*, 403(6766), 179–182.
- 778 Ledwell, J. R., & Watson, A. J. (1991). The santa monica basin tracer experiment:
779 A study of diapycnal and isopycnal mixing. *Journal of Geophysical Research: Oceans*, 96(C5), 8695–8718.
- 780 Ledwell, J. R., Watson, A. J., & Law, C. S. (1993). Evidence for slow mixing
781 across the pycnocline from an open-ocean tracer-release experiment. *Nature*,
782 364(6439), 701–703.
- 783 Lee, M.-M., Coward, A. C., & Nurser, A. G. (2002). Spurious diapycnal mixing of
784 the deep waters in an eddy-permitting global ocean model. *Journal of physical
785 oceanography*, 32(5), 1522–1535.
- 786 Lemarié, F., Debreu, L., Shchepetkin, A., & Mcwilliams, J. C. (2012). On the stabil-
787 ity and accuracy of the harmonic and biharmonic isoneutral mixing operators
788 in ocean models. *Ocean Modell.*, 52, 9–35. doi: 10.1016/j.ocemod.2012.04.007
- 789 Marchesiello, P., Debreu, L., & Couvelard, X. (2009). Spurious diapycnal mixing in
790 terrain-following coordinate models: The problem and a solution. *Ocean Mod-
791 elling*, 26(3-4), 156–169. doi: 10.1016/j.ocemod.2008.09.004
- 792 Marchesiello, P., McWilliams, J., & Shchepetkin, A. (2003). Equilibrium structure
793 and dynamics of the California Current System. *J. Phys. Oceanogr.*, 33(4),
794 753–783. doi: 10.1175/1520-0485(2003)33<753:ESADOT>2.0.CO;2
- 795 Mazloff, M. R., Cornuelle, B., Gille, S. T., & Wang, J. (2020). The importance of
796 remote forcing for regional modeling of internal waves. *Journal of Geophysical
797 Research: Oceans*, 125(2), e2019JC015623. doi: 10.1029/2019JC015623
- 798 Megann, A. (2018). Estimating the numerical diapycnal mixing in an eddy-
799 permitting ocean model. *Ocean Modelling*, 121, 19–33. doi: <https://doi.org/10.1016/j.ocemod.2017.11.001>
- 800 Molemaker, M. J., McWilliams, J. C., & Dewar, W. K. (2015). Submesoscale
801 instability and generation of mesoscale anticyclones near a separation of
802 the California Undercurrent. *J. Phys. Oceanogr.*, 45(3), 613–629. doi:
803 10.1175/JPO-D-13-0225.1
- 804 Munk, W., & Wunsch, C. (1998). Abyssal recipes II: Energetics of tidal and wind
805 mixing. *Deep Sea Research Part I: Oceanographic Research Papers*, 45(12),
806 1977–2010.
- 807 Naveira Garabato, A. C., Polzin, K. L., King, B. A., Heywood, K. J., & Visbeck, M.
808 (2004). Widespread intense turbulent mixing in the Southern Ocean. *Science*,
809 303(5655), 210–213.
- 810 Olbers, D., & Eden, C. (2013). A global model for the diapycnal diffusivity in-
811 duced by internal gravity waves. *Journal of Physical Oceanography*, 43(8),
812 1759–1779.
- 813 Osborn, T. R. (1980). Estimates of the local rate of vertical diffusion from dissipa-
814 tion measurements. *Journal of physical oceanography*, 10(1), 83–89.

- 817 Penven, P., Echevin, V., Pasapera, J., Colas, F., & Tam, J. (2005). Average circulation, seasonal cycle, and mesoscale dynamics of the Peru Current System: A modeling approach. *J. Geophys. Res.*, 110(C10), C10021. doi: 10.1029/2005JC002945
- 818 Piron, A., Thierry, V., Mercier, H., & Caniaux, G. (2017). Gyre-scale deep convection in the subpolar north atlantic ocean during winter 2014–2015. *Geophysical Research Letters*, 44(3), 1439–1447. doi: <https://doi.org/10.1002/2016GL071895>
- 819 Ruan, X., & Ferrari, R. (2021). Diagnosing diapycnal mixing from passive tracers. *Journal of Physical Oceanography*, 51(3), 757–767. doi: <https://doi.org/10.1175/JPO-D-20-0194.1>
- 820 Saha, S., Moorthi, S., Pan, H.-L., Wu, X., Wang, J., Nadiga, S., ... others (2010). The ncep climate forecast system reanalysis. *Bulletin of the American Meteorological Society*, 91(8), 1015–1058. doi: <https://doi.org/10.1175/2010BAMS3001.1>
- 821 Samelson, R., & Vallis, G. K. (1997). Large-scale circulation with small diapycnal diffusion: The two-thermocline limit. *Journal of Marine Research*, 55(2), 223–275.
- 822 Shchepetkin, A., & McWilliams, J. C. (2008). Computational kernel algorithms for finescale, multi-process, long-time oceanic simulations. *Handb. Numer. Anal.*, 14, 121–183.
- 823 Shchepetkin, A., & McWilliams, J. C. (2011). Accurate Boussinesq modeling with a practical, "stiffened" equation of state. , 34, 41–70.
- 824 Shchepetkin, A. F. (2015). An adaptive, courant-number-dependent implicit scheme for vertical advection in oceanic modeling. *Ocean Modelling*, 91, 38–69.
- 825 Shchepetkin, A. F., & McWilliams, J. C. (2003). A method for computing horizontal pressure-gradient force in an oceanic model with a nonaligned vertical coordinate. *Journal of Geophysical Research: Oceans*, 108(C3). doi: 10.1029/2001JC001047
- 826 Shchepetkin, A. F., & McWilliams, J. C. (2005). The regional oceanic modeling system (roms): a split-explicit, free-surface, topography-following-coordinate oceanic model. *Ocean Modelling*, 9(4), 347–404. Retrieved from <https://www.sciencedirect.com/science/article/pii/S1463500304000484> doi: <https://doi.org/10.1016/j.ocemod.2004.08.002>
- 827 Stewart, K., Hogg, A. M., Griffies, S., Heerdegen, A., Ward, M., Spence, P., & England, M. H. (2017). Vertical resolution of baroclinic modes in global ocean models. *Ocean Modelling*, 113, 50–65. Retrieved from <https://www.sciencedirect.com/science/article/pii/S1463500317300434> doi: <https://doi.org/10.1016/j.ocemod.2017.03.012>
- 828 Stommel, H. (1958). The abyssal circulation. *Deep-Sea Research*, 5(1), 80–82.
- 829 Taylor, G. (1922). Diffusion by continuous movements. *Proc. London Math. Soc.*, 2(1), 196–212.
- 830 Thakur, R., Arbic, B. K., Menemenlis, D., Momeni, K., Pan, Y., Peltier, W. R., ... Ma, Y. (2022). Impact of vertical mixing parameterizations on internal gravity wave spectra in regional ocean models. *Geophysical Research Letters*, 49(16), e2022GL099614. doi: 10.1029/2022GL099614
- 831 Tozer, B., Sandwell, D. T., Smith, W. H. F., Olson, C., Beale, J. R., & Wessel, P. (2019). Global bathymetry and topography at 15 arc sec: Srtm15+. *Earth and Space Science*, 6(10), 1847–1864. Retrieved from <https://agupubs.onlinelibrary.wiley.com/doi/abs/10.1029/2019EA000658> doi: <https://doi.org/10.1029/2019EA000658>
- 832 Vic, C., Ferron, B., Thierry, V., Mercier, H., & Lherminier, P. (2021). Tidal and near-inertial internal waves over the Reykjanes Ridge. *Journal of Physical Oceanography*, 51, 419–437. doi: 10.1175/JPO-D-20-0097.1
- 833 Vic, C., Gula, J., Roullet, G., & Pradillon, F. (2018). Dispersion of deep-sea hy-

- 872 hydrothermal vent effluents and larvae by submesoscale and tidal currents. *Deep-*
873 *Sea Research Part I*, 133, 1–18. doi: 10.1016/j.dsr.2018.01.001
- 874 Waterhouse, A. F., MacKinnon, J. A., Nash, J. D., Alford, M. H., Kunze, E., Sim-
875 mons, H. L., ... others (2014). Global patterns of diapycnal mixing from
876 measurements of the turbulent dissipation rate. *Journal of Physical Oceanogra-
877 phy*, 44(7), 1854–1872. doi: <https://doi.org/10.1175/JPO-D-13-0104.1>
- 878 Xu, X., Chassignet, E. P., & Wallcraft, A. J. (2023). Impact of vertical resolu-
879 tion on representing baroclinic modes and water mass distribution in the
880 North Atlantic. *Ocean Modelling*, 186, 102261. Retrieved from <https://www.sciencedirect.com/science/article/pii/S1463500323001014> doi:
881 <https://doi.org/10.1016/j.ocemod.2023.102261>
- 882 Zilberman, N., Becker, J., Merrifield, M., & Carter, G. (2009). Model estimates
883 of M_2 internal tide generation over Mid-Atlantic Ridge topography. *Journal of
884 Physical Oceanography*, 39(10), 2635–2651. doi: 10.1175/2008JPO4136.1
- 885

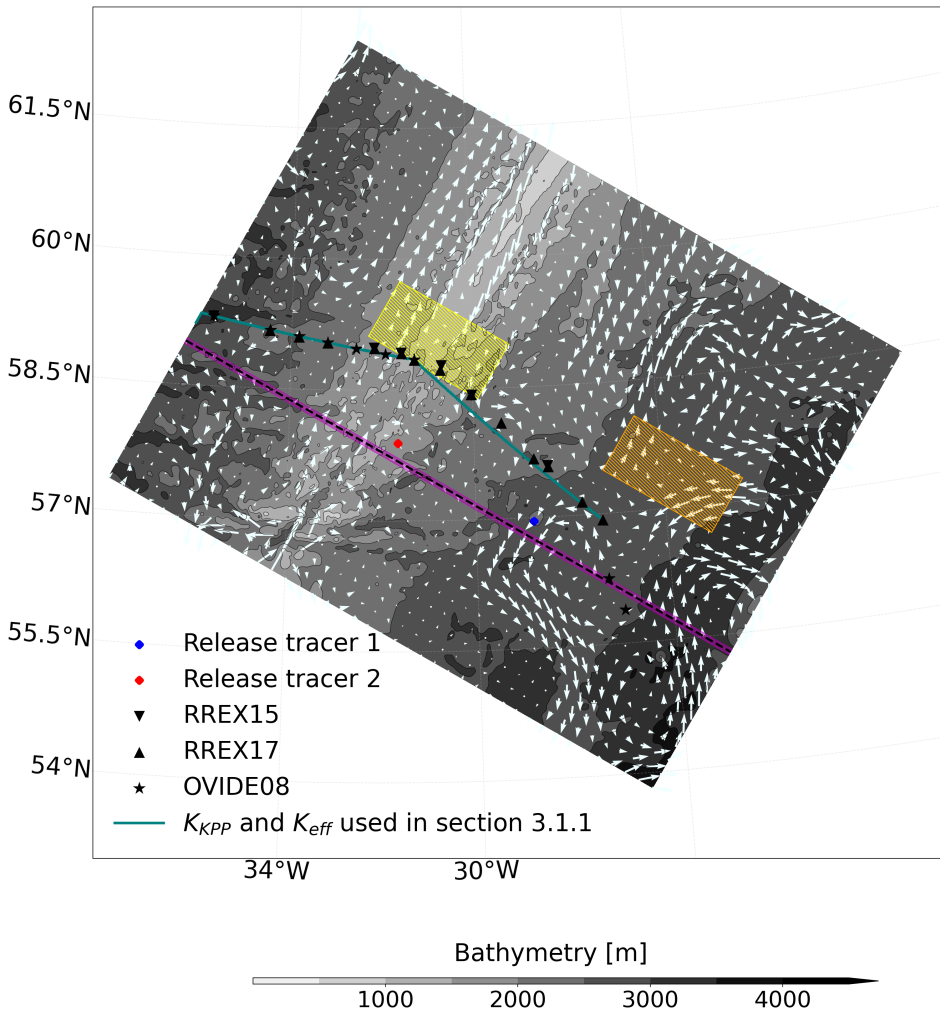


Figure 1. Top view of the Reykjanes Ridge and the model grid. Red and blue squares indicate the initial location of the passive tracer patches. Tracer patch 1 is released at $\rho = 1027.700 \text{ kg m}^{-3}$, while tracer patch 2 is released at $\rho = 1027.775 \text{ kg m}^{-3}$. The arrows represent the circulation at 1000 meters depth averaged over 40 days. The bathymetry of the grid is indicated by the white-black colorbar. The yellow and orange dashed areas are used to contrast the mixing profiles between the ridge and the abyssal plain in section 3.1. The black dashed line is the vertical section used in figures 2,3 and 6; the purple area represents the along ridge vertical sections used in figures 7 and 8.

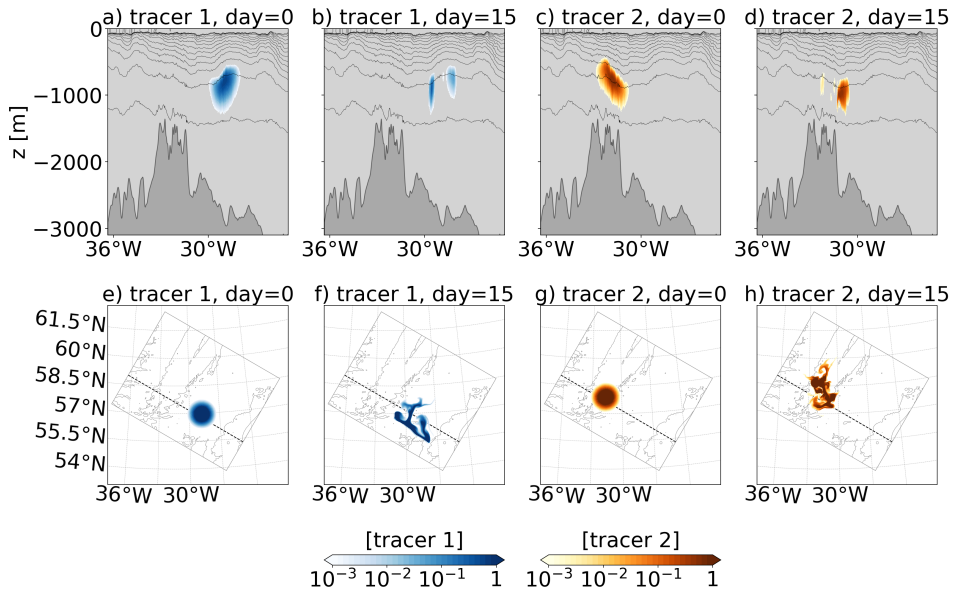


Figure 2. Vertical (a-d) and horizontal (e-h) snapshots of tracer concentration from the configuration exp200-rsup5 for a,e) tracer 1 at release, b,f) tracer 1 after 15 days, c,g) tracer 2 at release, and d,h) tracer 2 after 15 days. The solid black lines in the upper panels represent the potential density field referenced at the surface from 1026.5 kg.m^{-3} to 1028.4 kg.m^{-3} with variations of 0.1 kg m^{-3} . The vertical section used is the black dashed line in panels (e-h). Tracer patches are vertically integrated in the lower panels and the solid black lines represent the contour of the bathymetry every 1000 meters.

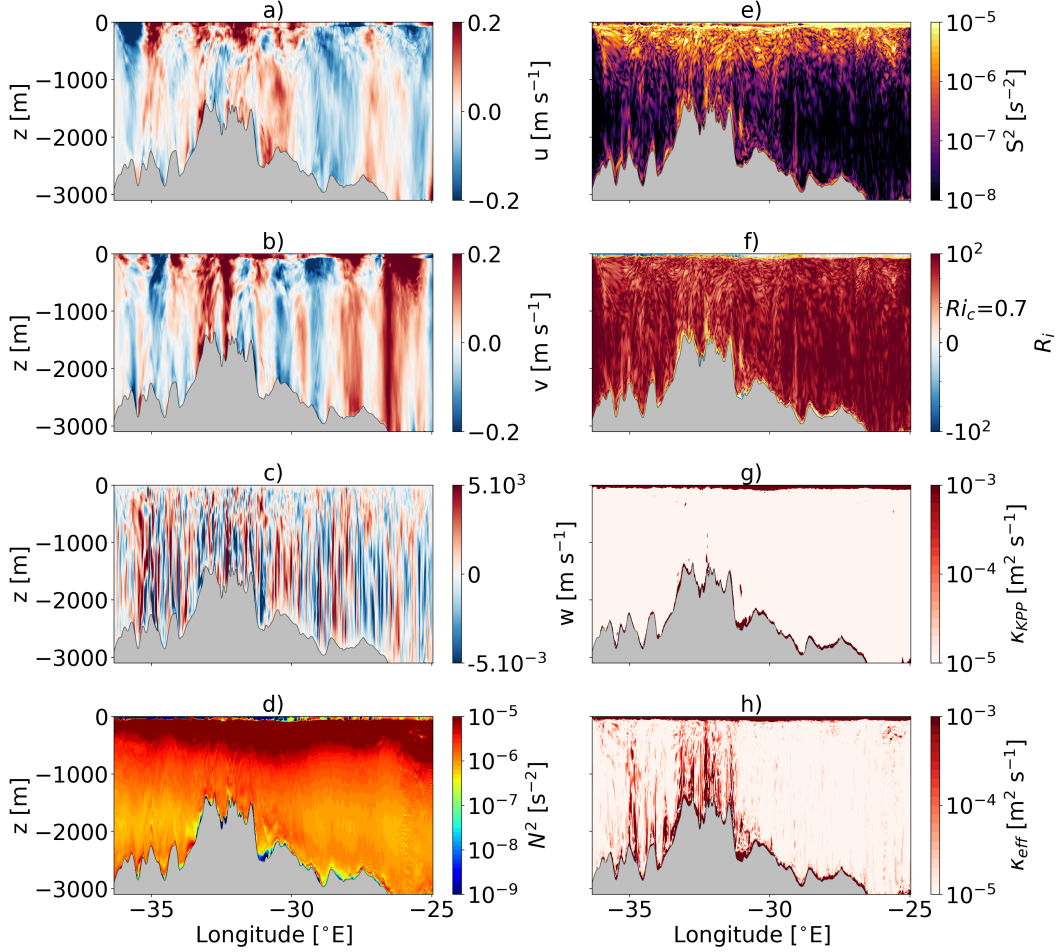


Figure 3. Vertical section of (a) zonal velocity u (in m/s), (b) meridional velocity v (in m/s), (c) vertical velocity w (in m/s), (d) Brunt-Vaisala frequency N^2 (in s⁻²), (e) vertical shear of horizontal velocity S^2 (in s⁻²), (f) Richardson number Ri , (g) the parameterised mixing K_{KPP} , and (h) the effective mixing K_{eff} for the exp200-rsup5 experiment 10 days after tracer release.

The vertical section is taken at the black dashed line in figure 1.

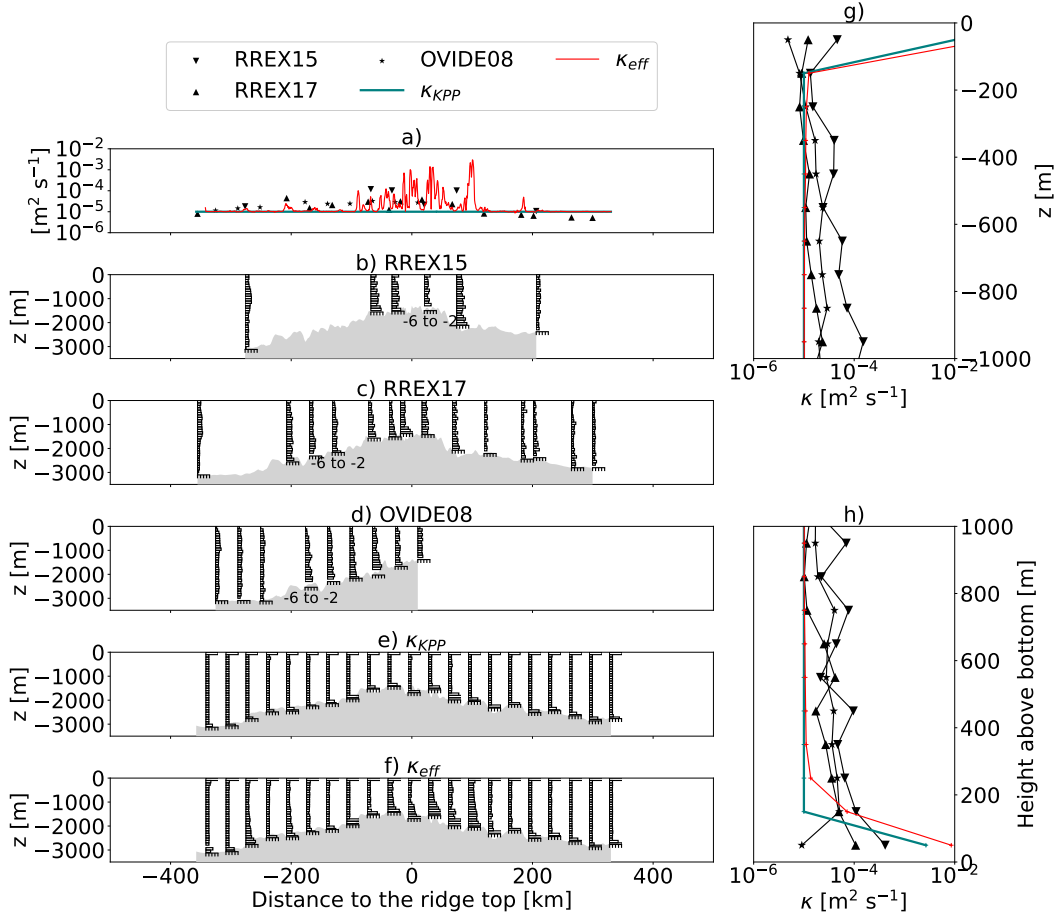


Figure 4. Comparison of observed diffusivities from campaigns RREX15, RREX17, and OVIDE08, with parameterized diffusivities from KPP and effective diffusivity K_{eff} in the exp200-rsup5 configuration along the blue section visible in figure 1. Median diffusivities as a function of (a) the distance to the ridge, (g) the depth and (h) the height above bottom for the RREX15, RREX17 and OVIDE08 campaigns, the KPP diffusivity, and the effective diffusivity K_{eff} . The median is computed over 29 days for K_{KPP} and K_{eff} . Vertical profiles of diffusivities estimated from (b) RREX15 (c) RREX17, and (d) OVIDE08 observations. Median values from 29 days of exp200-rsup5 for (e) the KPP diffusivity and (f) the effective diffusivity K_{eff} . The vertical profiles are shown every 20km in panels e) and f).

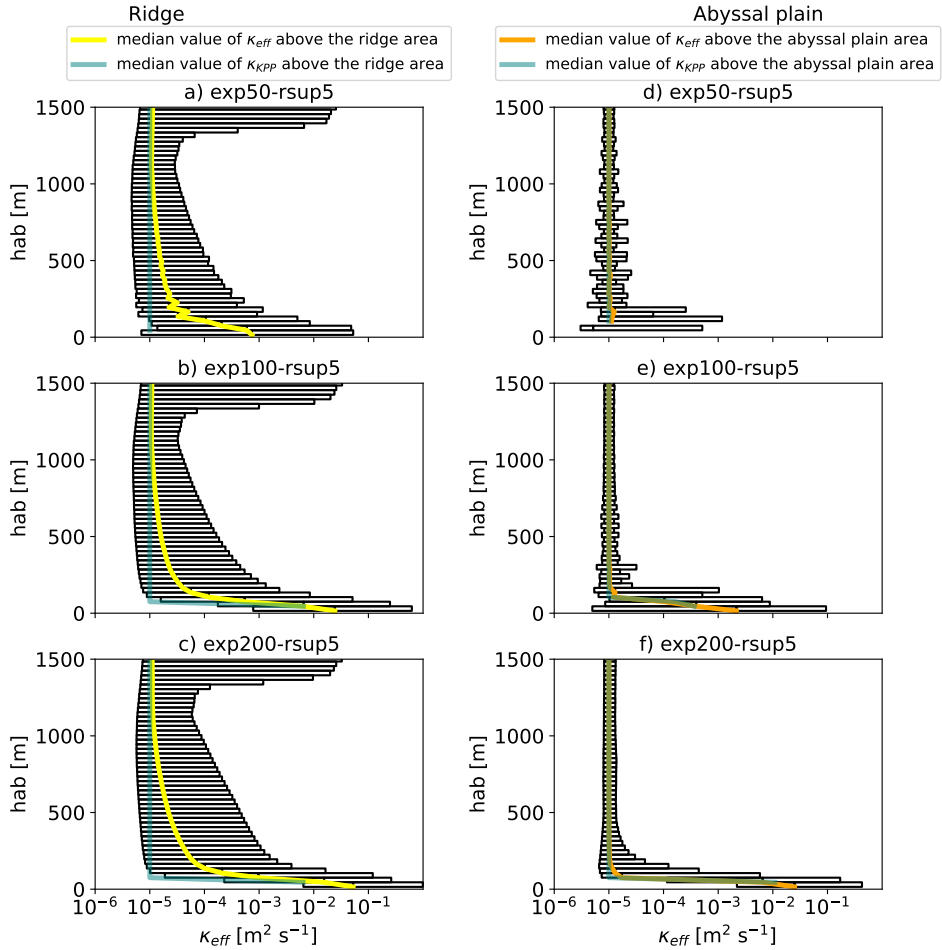


Figure 5. Effective mixing K_{eff} as a function of height above bottom averaged over (a,b,c) the ridge (yellow dashed rectangle on Fig. 1), and (d,e,f) the abyssal plain (orange dashed rectangle on Fig. 1) for configurations (a,d) exp50-rsup5, (b,e) exp100-rsup5, and (c,f) exp200-rsup5. The edges of the box represent the 10th and the 90th percentiles of K_{eff} for each height above bottom.

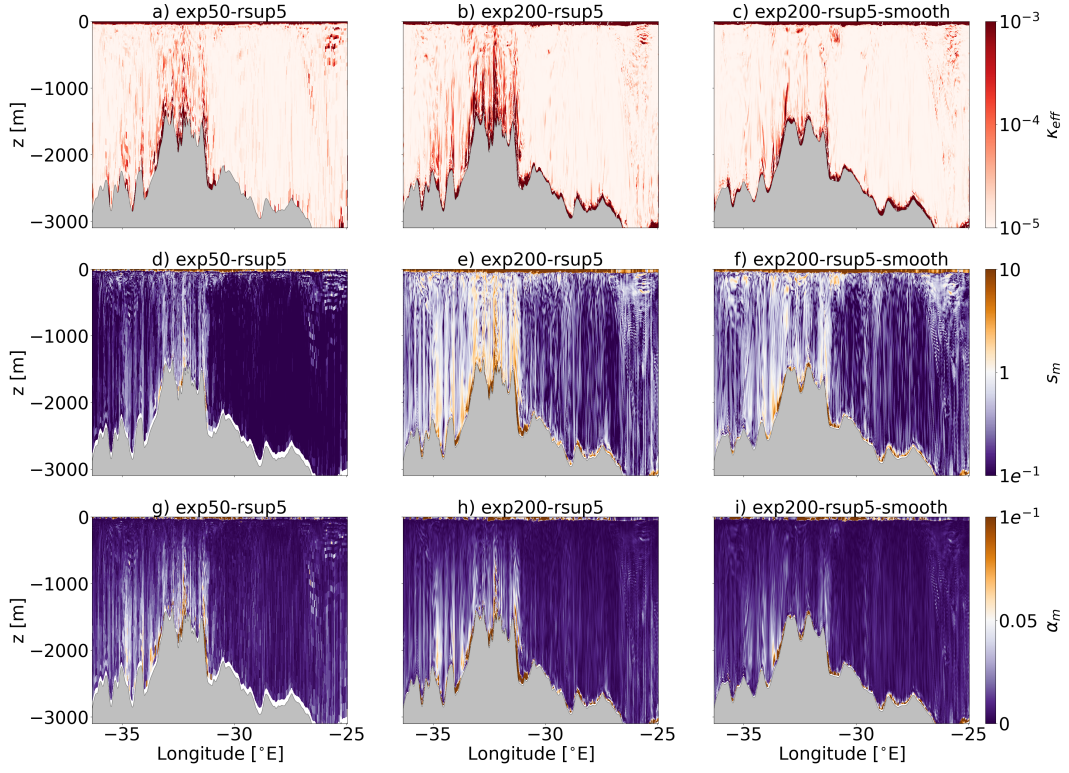


Figure 6. Snapshot at 10 days of vertical sections of (a)-(c) K_{eff} , (d)-(f) the grid slope ratio s_m , and (g)-(i) the maximum isopycnal slope α_m , for (a,d,g) exp50-rsup5, (b,e,h) exp200-rsup5, and (c,f,i) exp200-rsup5-smooth. The values $\alpha = 0.05$ and $s_m = 1$ are the critical values α_m and s_m . The vertical section is taken at the black dashed line in figure 1.

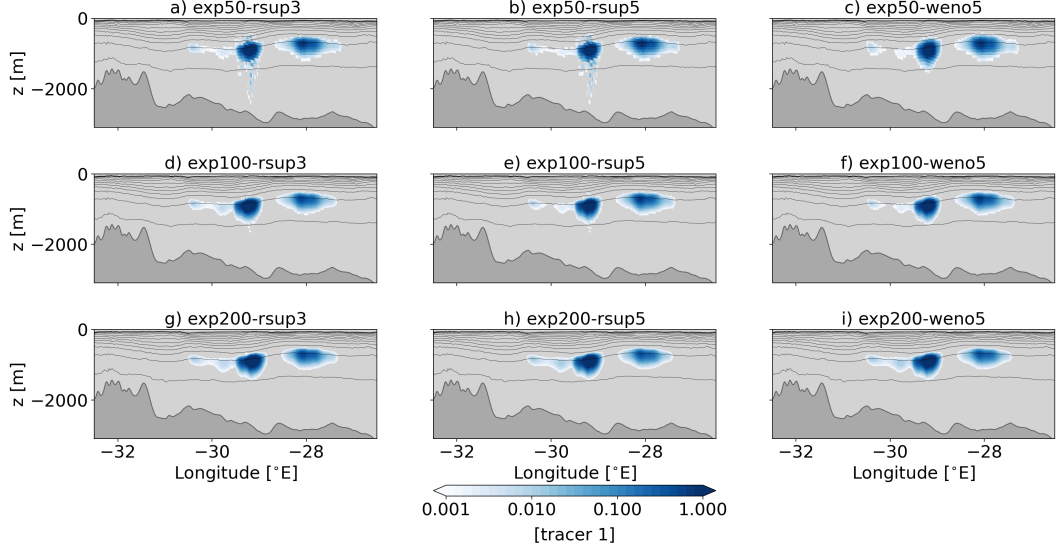


Figure 7. Vertical section of tracer 1 after 10 days for each configuration. The tracer patch is summed over 10 grid points in the along ridge direction indicated by the purple area in figure 1 and negative concentrations are not shown.

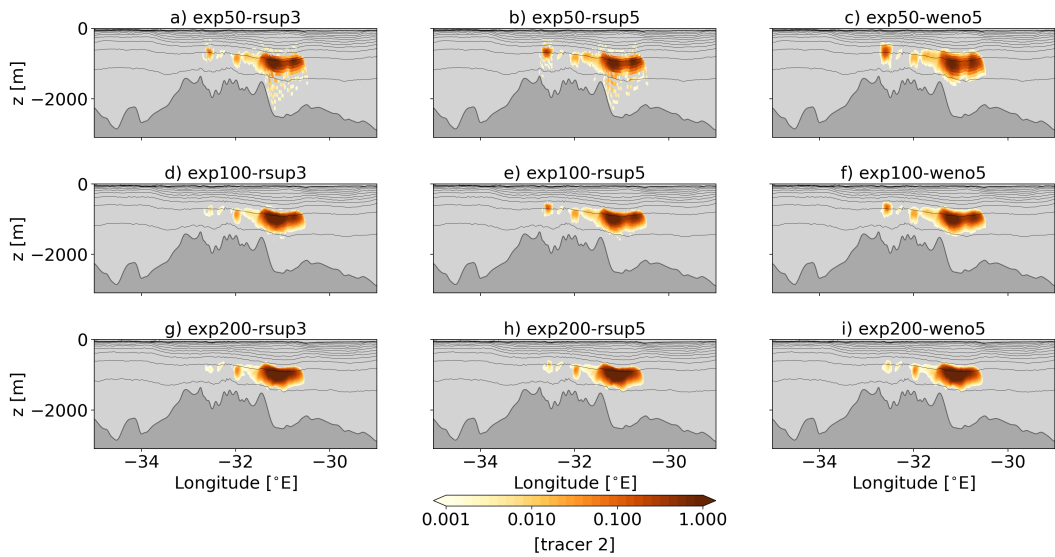


Figure 8. Vertical section of tracer 2 after 10 days for each configuration. The tracer patch is summed over 10 grid points in the along ridge direction. The location of the section corresponds to the purple area in figure 1 and negative concentrations are not shown.

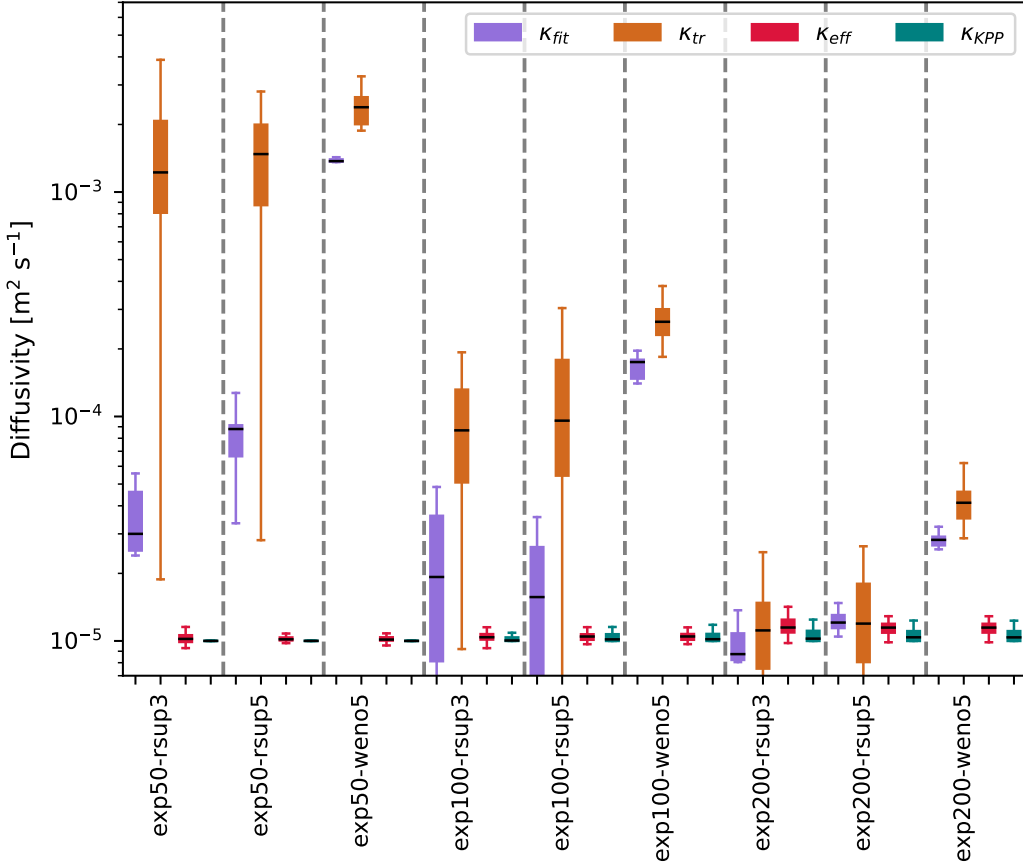


Figure 9. Estimation of the diffusivities experienced by tracer 1 for configurations exp50-rsup3, exp50-rsup5, exp50-rweno5, exp100-rsup3, exp100-rsup5, exp100-rsweno5, exp200-rsup3, exp200-rsup5, exp200-rsweno5. The parameterised diffusivity K_{KPP} is in blue, the online diagnosed effective diffusivity K_{eff} is in red, and the two tracer-based diffusivities K_{tr} and K_{fit} are in orange and purple. K_{eff} and K_{KPP} are weighted by the tracer concentration following Equ. 3. Diffusivities are considered for the first 15 days. For each box plot, the extremities of the box represent the minimum and the maximum values of the distribution and the box shows the first quartile, the median and the third quartile of the distribution. Concentrations of tracer less than $1e-6 \text{ m}^2 \text{ s}^{-1}$ are ignored in the calculation of diffusivities. K_{fit} is considered on the last 10 days because it encounters time adjustment on the first 5 days (see fig. 10).

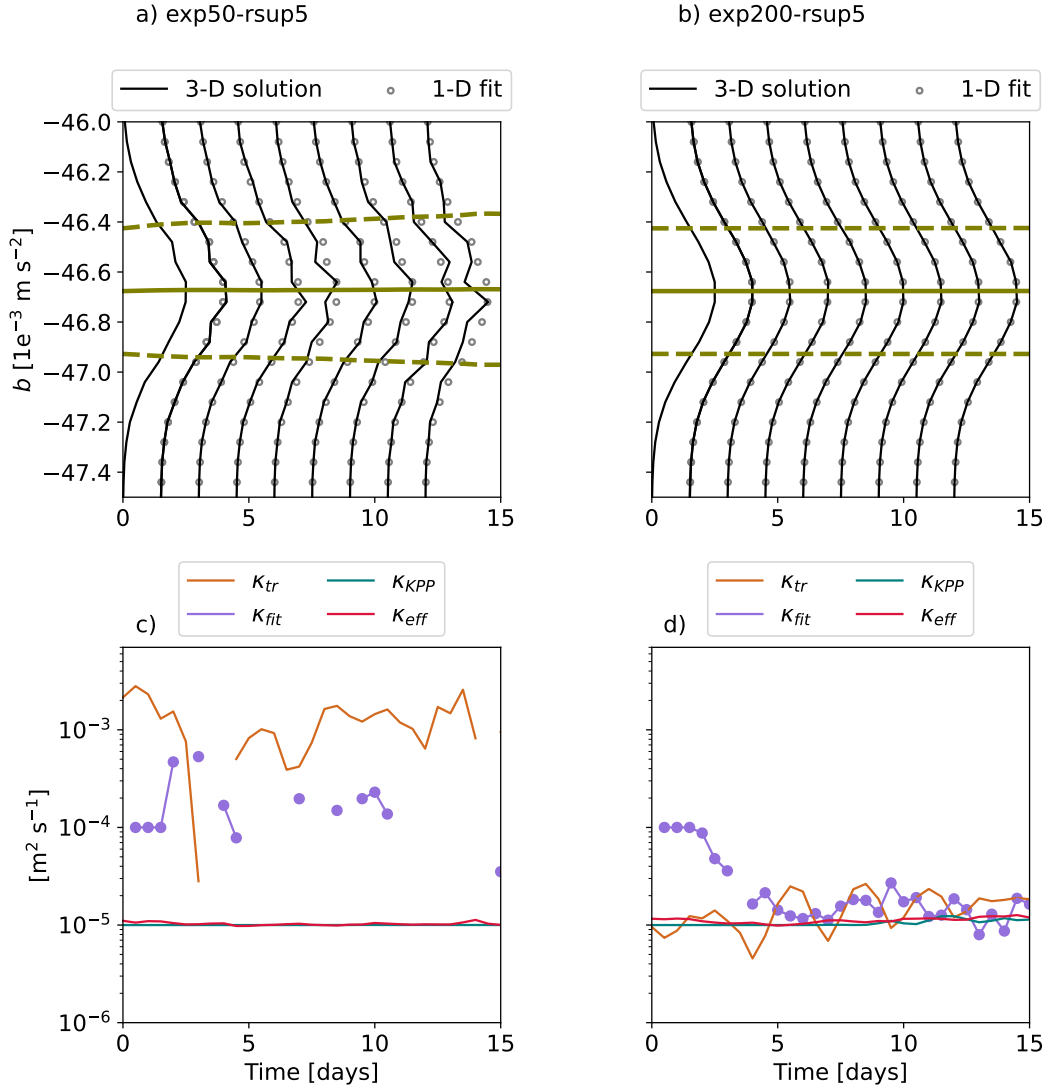


Figure 10. a,b) tracer 1 concentration binned in buoyancy space (black line) and one-dimensional fit used to compute K_{fit} (dot markers) for configurations a) exp50-rsup5 and b) exp200-rsup5. Green lines show the centre of gravity (plain) and the standard deviation (dashed) for the one-dimensional fit (equation 4). The lower panels show for configurations c) exp50-rsup5 and d) exp200-rsup5 the time evolution of diffusivities experienced by tracer 1: the parameterised diffusivity K_{KPP} (blue line), the online diagnosed effective diffusivity K_{eff} in red, and the offline diagnosed effective diffusivities K_{tr} and K_{fit} (orange and purple lines). Concentrations of tracer less than $1\text{e}-6$ are not considered here.

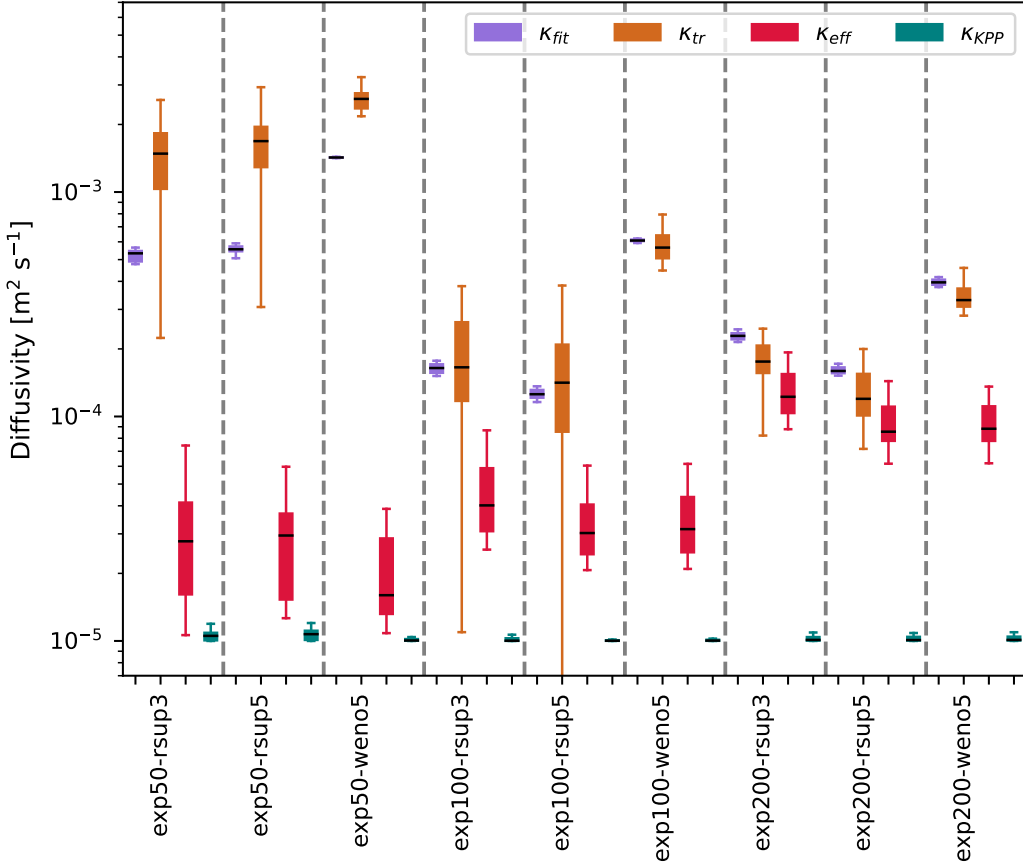


Figure 11. Estimation of the diffusivities experienced by tracer 2 for configurations exp50-rsup3 , exp50-rsup5 , exp50-rweno5 , exp100-rsup3 , exp100-rsup5 , exp100-rsweno5 , exp200-rsup3 , exp200-rsup5 , exp200-rsweno5 . The parameterised diffusivity K_{KPP} is in blue, the online diagnosed effective diffusivity K_{eff} is in red, and the two tracer-based diffusivities K_{tr} and K_{fit} are in orange and purple. K_{eff} and K_{KPP} are weighted by the tracer concentration following Equ. 3. Diffusivities are considered for the first 15 days. For each box plot, the extremities of the box represent the minimum and the maximum values of the distribution and the box shows the first quartile, the median and the third quartile of the distribution. Concentrations of tracer less than $1\text{e-}6 \text{ m}^2 \text{ s}^{-1}$ are ignored in the calculation of diffusivities. K_{fit} is considered on the last 10 days because it encounters time adjustment on the first 5 days (see fig. 10).

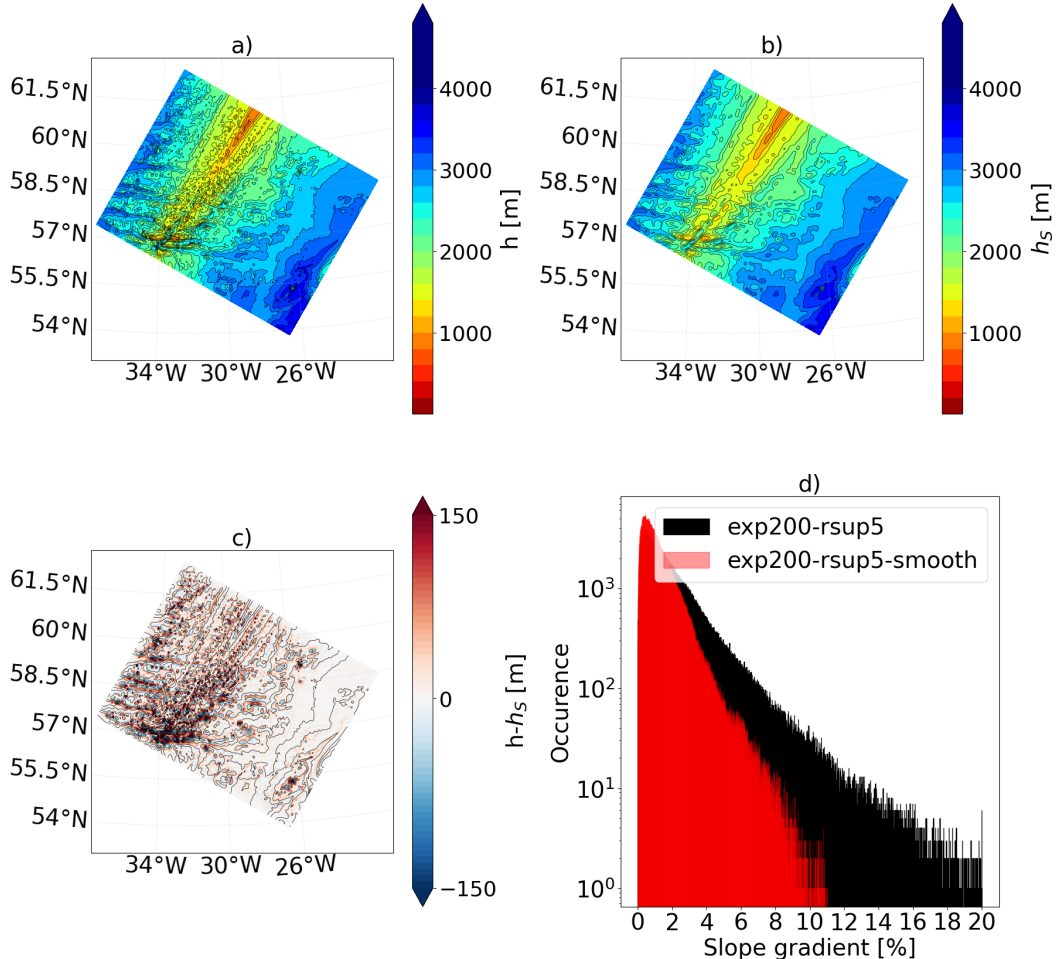


Figure 12. (a) Reference bathymetry and (b) smoothed bathymetry used in exp-200-rsup5-smooth (c) difference between reference and smoothed bathymetries and (d) histogram of the slope gradient with the unsmoothed topography displayed over the exp200-rsup5 configuration (black histogram) and the smoothed topography used in the exp200-rsup5-smooth configuration (light red histogram). The black lines are the contour each 200m of the reference bathymetry (panels a) and c)) and of the smoothed bathymetry (panel b)).

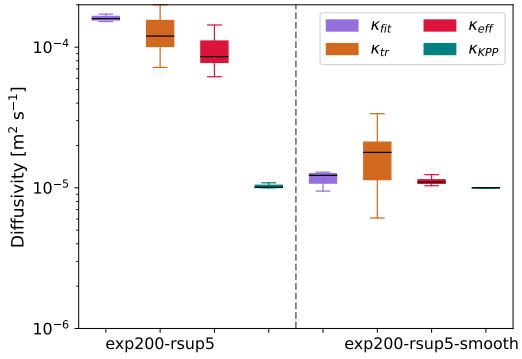


Figure 13. Diffusivities experienced by tracer 2 for configurations exp200-rsup5 and $\text{exp200-rsup5-smooth}$. The parameterised diffusivity K_{KPP} is in blue, the effective diffusivity K_{eff} is in red, and the two tracer-based diffusivities K_{tr} and K_{fit} are in orange and purple. K_{eff} and K_{KPP} are weighted by the tracer concentration following Equ. 3. Diffusivities are considered for the first 15 days. For each box plot, the extremities of the box represent the minimum and the maximum values of the distribution and the box shows the first quartile, the median and the third quartile of the distribution. Concentrations of tracer less than $1\text{e-}6 \text{ m}^2 \text{ s}^{-1}$ are not considered when computing diffusivities. K_{fit} is considered on the last 10 days because it encounters time adjustment on the first 5 days (see fig. 10).

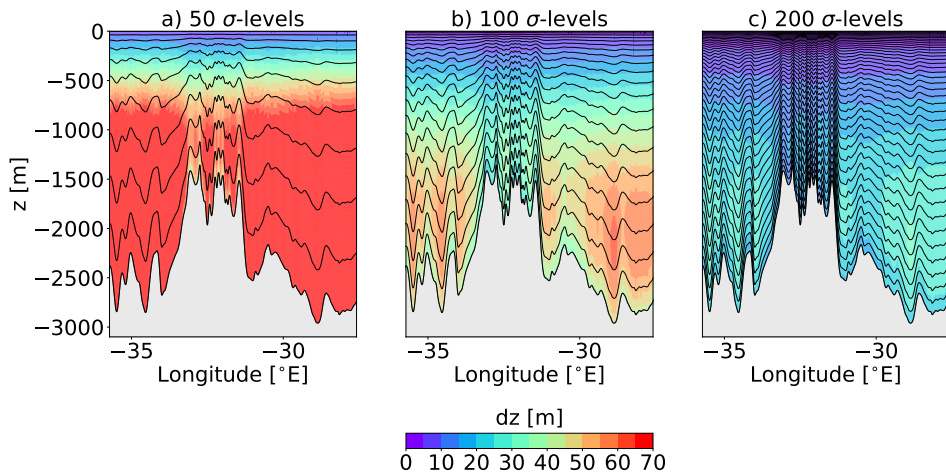


Figure A1. Vertical resolution [m] using (a) exp50-rsup5 (b) exp100-rsup5 and (c) exp200-rsup5 . The vertical section is taken at the black dashed line in figure 1.

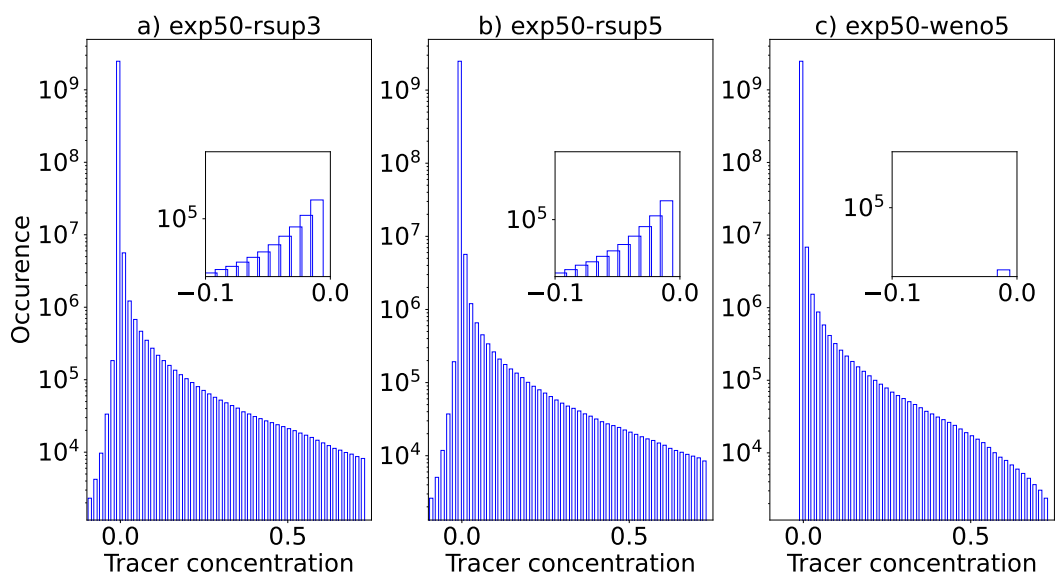


Figure B1. Histogram of tracer 1 concentration over 40 days for configurations: a) exp50-up3
b) exp50-rsup5 and c) exp50-weno5

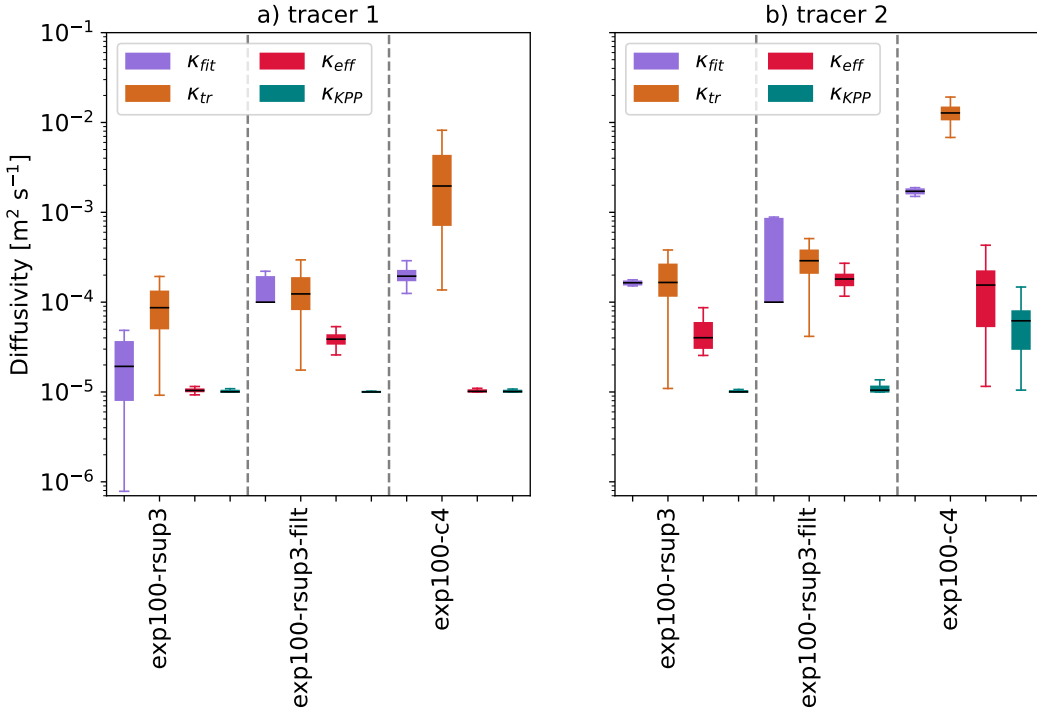


Figure C1. Estimation of the diffusivities experienced by a) the tracer 1 and b) the tracer 2 for configurations exp100-rsup3, exp100-rsup3-filt and exp100-c4. The parameterised diffusivity is in blue, the effective diffusivity K_{eff} is in red, and the two tracer-based diffusivities K_{tr} and K_{fit} are in orange and purple. K_{eff} and K_{KPP} are weighted by the tracer concentration following Equ. 3. Diffusivities are considered for the first 15 days. For each box plot, the extremities of the box represent the minimum and the maximum values of the distribution and the box shows the first quartile, the median and the third quartile of the distribution. Concentrations of tracer less than $1e-6 \text{ m}^2 \text{ s}^{-1}$ are not considered when computing diffusivities. K_{fit} is considered on the last 10 days.